

Hadley Centre
for Climate Predictions and Research



Estimation of natural and anthropogenic contributions to 20th Century Temperature Change

by:

SIMON F. B. TETT, GARETH S. JONES, PETER A. STOTT,
DAVID C. HILL[†], JOHN F. B. MITCHELL, MYLES R. ALLEN^{†‡}, WILLIAM J. INGRAM,
TIM C. JOHNS, COLIN E. JOHNSON, ANDY JONES,
DAVID L. ROBERTS, DAVID M. H. SEXTON AND MARGARET J. WOODAGE

*Hadley Centre for Climate Prediction and Research,
The Met. Office, London Road, Bracknell, Berkshire RG12 2SY, UK.
[†]Space Science and Technology Dept., Rutherford Appleton Laboratory,
Chilton, OX11 0QX, UK*

[‡]Dept. of Physics, Clarendon Laboratory, University of Oxford, Oxford, OX1 3PU, UK

HCTN 19

Hadley Centre Technical Note

October 2000



The Met.Office

Estimation of natural and anthropogenic contributions to 20th Century Temperature Change

SIMON F. B. TETT, GARETH S. JONES, PETER A. STOTT,
DAVID C. HILL[†], JOHN F. B. MITCHELL, MYLES R. ALLEN^{†‡}, WILLIAM J. INGRAM,
TIM C. JOHNS, COLIN E. JOHNSON, ANDY JONES,
DAVID L. ROBERTS, DAVID M. H. SEXTON AND MARGARET J. WOODAGE

Hadley Centre for Climate Prediction and Research,

The Met. Office, London Road, Bracknell, Berkshire RG12 2SY, UK.

[†]*Space Science and Technology Dept., Rutherford Appleton Laboratory,
Chilton, OX11 0QX, UK*

[‡]*Dept. of Physics, Clarendon Laboratory, University of Oxford, Oxford, OX1 3PU, UK*

Abstract

Using a coupled atmosphere/ocean general circulation model we have simulated the climatic response to natural and anthropogenic forcings from 1860 to 1997. The model, HadCM3, requires no flux adjustment, and has an interactive sulphur cycle, a simple parametrisation of the effect of aerosols on cloud albedo (first indirect effect) and a radiation scheme which allows explicit representation of well-mixed greenhouse gases. Simulations were carried out in which the model was forced with: changes in natural forcings (solar irradiance and stratospheric aerosol due to explosive volcanic eruptions); well-mixed greenhouse gases alone; tropospheric anthropogenic forcings (tropospheric ozone, well-mixed greenhouse gases and the direct and first indirect effects of sulphate aerosol); anthropogenic forcings (tropospheric anthropogenic forcings and stratospheric ozone decline).

Using an “optimal detection” methodology to examine temperature changes near the surface and throughout the free atmosphere we find that we can detect the effects of changes in well-mixed greenhouse gases, other anthropogenic forcings and natural forcings. Thus these have all had a significant impact on temperature. We estimate the linear trend in global-mean near-surface temperature from well mixed greenhouse gases to be 0.9 ± 0.24 K/century, offset by cooling from other anthropogenic forcings of 0.4 ± 0.26 K/century giving a total anthropogenic warming trend of 0.5 ± 0.15 K/century. Over the entire century natural forcings give a linear trend close to zero. Observed surface temperature changes are generally consistent with our simulations but the simulated tropospheric response, since the 1960s, is about 50% too large.

Our analysis suggests that the early 20th century warming can best be explained by a combination of warming due to increases in greenhouse gases and natural forcing, some cooling due to other anthropogenic forcings, plus a substantial, but not implausible, contribution from internal variability. In the second half of the century we find that the warming is largely caused by changes in greenhouse gases, with changes in sulphates and, perhaps, volcanic aerosol offsetting approximately one-third of the warming. Warming in the troposphere, since the 1960s, is probably mainly due to anthropogenic forcings with a negligible contribution from natural forcings.

1 Introduction

Several authors (e.g. *Santer et al.* [1996]; *Hegerl et al.* [1997]; *North and Stevens* [1998]; *Tett et al.* [1999]; *Hegerl et al.* [2000b]; *Stott et al.* [2000]) have carried out studies in which they claimed to have detected significant changes in temperature either at the surface or in the free atmosphere. On decadal timescales or longer they attributed changes over the last 30-50 years to anthropogenic rather than natural effects whether externally forced or due to internal variability. Most of these studies used a variant of the optimal fingerprinting algorithm [*Hasselmann*, 1993; *North et al.*, 1995; *North and Kim*, 1995; *Hasselmann*, 1997; *Hegerl and North*, 1997; *Allen and Tett*, 1999].

Tett et al. [1999] (T99 from hereon) and *Stott et al.* [2000] (S00 from hereon) computed responses from the Atmosphere/Ocean General Circulation Model (AOGCM) HadCM2 [*Johns et al.*, 1997] to solar, volcanic, greenhouse and the direct anthropogenic sulphate forcing. They compared the responses with observations of surface temperature using a spatio-temporal methodology and concluded that natural causes alone could not explain observed changes in surface temperature from 1946–1996. HadCM2 included an ocean model with a resolution of $2.5^\circ \times 3.75^\circ$ and needed a flux adjustment¹ to keep the control simulation stable and its climate close to the current climate. It represented all greenhouse gases as equivalent CO₂, and the direct effect of sulphates as changes in surface albedo.

Barnett et al. [1999] compared simulations from several different models with observations and found that there were cases in which simulated linear trends in northern summer temperature were inconsistent with observations. Most of those models used a simple parametrisation of the effects of sulphate aerosols similar to that used in HadCM2. However they found that the amplitude of the “sulphate” component computed from a single simulation of ECHAM4 (a model with a representation of the indirect effect of aerosols and an interactive sulphur cycle) was, in one case, inconsistent with observations. If this result were confirmed by other models, which include physically based parametrisations of the direct and indirect effect of sulphates, then the hypothesis that sulphates alone have significantly offset greenhouse gas warming would be unlikely to be

¹ Flux adjustments are artificial fluxes of heat and water which vary in space and throughout the seasonal cycle but are constant from year to year and in all the HadCM2 simulations.

true.

The aim of this paper is to examine the contributions of natural and anthropogenic forcings to temperature change during the 20th century using a new AOGCM, HadCM3[Gordon *et al.*, 2000; Pope *et al.*, 2000]. HadCM3 has 19 atmospheric levels with a resolution of $2.5^\circ \times 3.75^\circ$ and the ocean component has 20 levels with a resolution of $1.25^\circ \times 1.25^\circ$. In addition to an increase in oceanic resolution it includes many improvements on HadCM2 which have removed the need for a flux adjustment. HadCM3 represents the radiative effects of CO₂, N₂O, CH₄, and some of the (H)(C)FCs individually. The direct effect of sulphate aerosol is now simulated using a fully interactive sulphur cycle scheme that models the emissions, transport, oxidation and removal of sulphur species. The first indirect effect of sulphate aerosol[Twomey, 1974], which was not represented at all in HadCM2, is now modelled using a relatively simple, non-interactive technique.

The control simulation is stable for multi-century integrations and the temperature variability near the surface, though not in the free atmosphere, compares well with observations[Collins *et al.*, 2000b]. HadCM2 and HadCM3 show similar global-mean temperature responses to increases in greenhouse gases during the 20th and the 21st centuries but HadCM3 shows less tropical warming than HadCM2 due to changes in details of the physics parametrisations[Williams *et al.*, 2000].

We present an analysis based on changes in near-surface temperature change from 1897–1997. In order to compare results with earlier work using HadCM2 we also consider changes in near-surface temperature on 50-year timescales as in T99 and S00, and changes in the temperature of the free atmosphere on 35-year timescales (Tett *et al.* [1996] (T96 from hereon) and Allen and Tett [1999] (AT99 from hereon)).

The rest of the paper is organised as follows. First we describe the simulations, radiative forcings and observations. We then describe the simulated responses and compare them with observations. Next we describe the detection and attribution methodology. In section 5 we show the results of the analyses and in section 6 we conclude.

2 Simulations

The control simulation for HadCM3 (CONTROL) has constant, near pre-industrial², forcing and we use the first 1200 years of the simulation in our analysis. Four ensembles with different external forcings were carried out using HadCM3. Each ensemble consisted of four simulations. The ensembles are:

GHG The simulations were forced with historical changes in well-mixed greenhouse gases.

TROP-ANTHRO The simulations were forced with changes in well-mixed greenhouse gases (as GHG), anthropogenic sulphur emissions and their implied changes to cloud albedos, and tropospheric ozone.

ANTHRO As TROP-ANTHRO except from 1974 stratospheric ozone decline was included.

NATURAL The simulations were forced with the solar irradiance timeseries of Lean *et al.* [1995a] and a timeseries of stratospheric aerosol due to explosive volcanic eruptions [Sato *et al.*, 1993]. Both forcing timeseries have been extended to 1997.

Four sets of initial conditions to start the GHG, ANTHRO and NATURAL ensembles were taken from states in CONTROL separated by 100 years. Note that, for example, the first GHG and NATURAL simulations use the same initial conditions. All simulations except TROP-ANTHRO start in 1/Dec/1859 and the twelve anthropogenic simulations ended on 30/Nov/1999. The NATURAL simulations were integrated to 30/Nov/1997. Initial conditions for TROP-ANTHRO were taken from ANTHRO on 1/Dec/1974.

2.1 Forcing factors

Well-mixed greenhouse gases CO₂, CH₄, N₂O and six (H)(C)FCs (CF₂Cl₂, CFCl₃, CF₃CFH₂, CHF₂Cl, CF₂ClCFCl₂ and C₂HF₅) were included with constant mass mixing ratios everywhere. Historical values were used to 1990[Schimel *et al.*, 1995]. From 1990 to 2000 the *preliminary* B2 SRES (Special Report on Emis-

²The concentrations (ppbv) used for the well-mixed greenhouse gases are: CO₂: 289600, CH₄: 792.1 N₂O: 285.1. The (H)(C)FCs all had zero concentrations.

sion Scenarios) scenario³ was used [Nakićenović *et al.*, 2000]. See Johns *et al.* [2000] for more details.

Sulphates In the ANTHRO and TROP-ANTHRO simulations, the model's interactive sulphur cycle scheme (described in Jones *et al.* [1999]) was used to compute the distribution of anthropogenic sulphate aerosol, which was then passed to the model's radiation scheme [Edwards and Slingo, 1996] for computation of its direct radiative effect. No natural emissions were included, as we assumed that the natural background of tropospheric sulphate aerosol was constant.

Estimates of the anthropogenic SO₂ emissions were taken from Orn *et al.* [1996] for 1860–1970, the GEIA 1B dataset for 1985 and the preliminary IPCC SRES datasets for 1990 and 2000 [Nakićenović *et al.*, 2000] and linearly interpolated between these times. As the distribution of sulphate aerosol is influenced by the height at which SO₂ emissions occur, we assumed that a fraction of the emissions originate from elevated sources such as power station chimneys. This fraction depends on location and from 1985 onwards is prescribed using the information in the GEIA 1B dataset. Before 1950 it is assumed to be zero, and between 1950 and 1985 the fraction is linearly interpolated in time.

CONTROL had fixed cloud droplet number concentrations and our simulations included only anthropogenic sulphur emissions. Thus we computed the indirect effect of anthropogenic sulphates on cloud albedo using two sets of offline simulations of a modified version of HadAM3 (the atmospheric component of HadCM3). Both sets of simulations used present-day concentrations of well-mixed greenhouse gases and seasonally varying SSTs. The first set used anthropogenic emissions of sulphur for 1860, 1900, 1950, 1975 and 2000, as well as natural emissions, to compute annual-mean distributions of sulphate aerosols for these years. The second set of offline simulations was run with the radiation scheme being called twice using aerosol distributions calculated by the previous set of simulations as input to these two calls. These aerosol distributions change the three-dimensional distribution of cloud albedo by affecting the cloud droplet concentrations seen by the radiation scheme. The difference in cloud albedo between the two radiation calls is a measure of the indirect effect of the difference between

the two aerosol distributions. This set of offline runs was used to generate a timeseries of three-dimensional changes in cloud albedo caused by the indirect effect. These fields were then annual-averaged, linearly interpolated in time, and used in the HadCM3 simulations to modify the albedo of the clouds so as to simulate the indirect effect.

In the HadCM3 simulations the radiative forcing due to the indirect effect is about 60–70% of that in the atmosphere-only simulations used to compute the albedo perturbations because the meteorology is different in the coupled and atmospheric simulations. Cloud albedo perturbations applied to a region in HadCM3 which, unlike the HadAM3 simulations, has no cloud, will clearly have no effect. In areas where the coupled simulation has cloud but the atmosphere-only simulation does not, there will again be no albedo perturbation applied, as clouds are needed in the atmosphere-only simulation to generate this perturbation.

A separate study [Jones *et al.*, 1999] using HadAM3 with an improved cloud microphysics parametrisation [Wilson and Ballard, 1999] driven by both natural and anthropogenic sulphur emissions, suggested that the model has roughly half the near-surface concentration of anthropogenic sulphate aerosol, compared with data from an European network (EMEP). This implies that the direct forcing due to anthropogenic sulphate is less than in reality. However, because the size of the indirect effect is related non-linearly to the difference between the natural background and anthropogenically perturbed aerosol, underestimating the true aerosol concentration could increase (less natural background) or decrease (smaller increase in aerosol) the indirect forcing.

More details on the parametrisation of the direct and indirect effects of sulphates in HadCM3 can be found in Johns *et al.* [2000].

Tropospheric ozone Three dimensional fields of monthly-mean tropospheric ozone were computed using the STOCHEM chemical model [Collins *et al.*, 1997] for 1860, 1900, 1950, 1975, 1990 and 2000. Values of ozone between those years were interpolated by assuming linearity between increases in observed methane concentration and modelled tropospheric ozone for each month in the year. Estimates of historical anthropogenic emissions of NO_x, CO, CH₄, and VOCs were obtained by scaling their present day emissions to the estimated time variation

³Differences between any of the SRES scenarios only occur from 2000 on but as we use linear interpolation to obtain intermediate values then our “historical” values will be affected by the 2000 values.

of NO_x emissions of *Dignon and Hameed* [1990]. Biomass burning emissions were estimated by assuming they were proportional to population. Below the mean model-diagnosed tropopause⁴ the anomalies from STOCHEM's pre-industrial values were zonally averaged, interpolated to HadCM3's levels, and then added to the HadCM3 pre-industrial values. Ozone concentrations above and on the tropopause were set to estimated pre-industrial values.

Stratospheric ozone From 1975 to 1979 half the SPARC trends [*Randel and Wu*, 1999] of stratospheric ozone, for each month of the annual cycle, were added to annual cycle of pre-industrial ozone above the mean model-diagnosed tropopause. After 1979, when stratospheric ozone decline is believed to have accelerated, the full SPARC trends were added. Ozone mass mixing ratios below 10^{-11} were set to 10^{-11} .

Volcanic aerosol The updated timeseries of volcanic aerosol depth due to *Sato et al.* [1993] was distributed above the model tropopause assuming a uniform mass mixing ratio. Note that the tropopause was diagnosed as the simulations proceeded, not prescribed as for the ozone changes.

Solar irradiance changes Changes in solar irradiance, as estimated by *Lean et al.* [1995a], were applied to the model by varying the "solar constant" in the model's radiation scheme with the changes spread over the solar spectrum following *Lean et al.* [1995b]. This allows for the effects of ozone absorption but not for the possibly larger effects due to changes in ozone [*Haigh*, 1994; *Haigh*, 1996].

2.2 Simulated forcings

Simulated forcings were computed for the various factors, using a diagnosed tropopause whose height can change (see Appendix B for details). The forcing due to greenhouse gases reaches a maximum of more than 2 W/m^2 by 2000 (Fig. 1(a)). By contrast, the total anthropogenic forcing reaches a maximum of approximately 0.8 W/m^2 , while the forcing due to tro-

pospheric anthropogenic forcings reaches a maximum value of almost 1.5 W/m^2 in 2000. The difference between the two is due to a strong negative forcing from stratospheric ozone decline. Using 1998 conditions we found that the forcing due to stratospheric ozone was $-0.5 \pm 0.1 \text{ W/m}^2$. When we repeated these calculations using a fixed tropopause the ozone forcing increased to -0.3 W/m^2 . We plan to investigate this difference in more detail in subsequent work.

Natural forcings from about 1910 to 1950 show a general increase due to an increase in solar irradiance and a lack of large volcanic effects after the 1912 Katmai eruption. Apparent in this timeseries is the solar cycle and large negative excursions due to the eruptions of Agung (1963), El Chichón (1982), Pinatubo (1991) and other volcanoes. Pinatubo causes the largest negative forcing of the 20th century with, in 1991, an annual-average global-mean forcing of -2.5 W/m^2 which, when added to a solar forcing of approximately 0.5 W/m^2 , gives a total natural forcing of -2 W/m^2 . The forcing due to volcanoes in HadCM3, after stratospheric adjustment, is approximately 20 W/m^2 per unit optical depth, less than the 30 W/m^2 (without adjustment) per unit optical depth quoted by *Lacis et al.* [1992]. This suggests a high degree of uncertainty in radiative forcing due to volcanic aerosol. Total natural and anthropogenic forcing shows a complex structure with a general slow increase until the 1960s after which total forcing is approximately constant though punctuated by volcanic eruptions.

The negative forcing due to the direct effect of sulphates is very small and largely balanced by the small positive forcing due to tropospheric ozone changes (Fig. 1(a)). There are two large negative forcings: that due to the indirect effect of sulphate aerosols and that due to stratospheric ozone. Both of these are highly uncertain [*Schimel et al.*, 1995]. With the exception of stratospheric ozone our computed anthropogenic forcings are all within the ranges quoted by *Schimel et al.* [1995].

Ten-year smoothed natural forcings (Fig. 1(b)) reached their maximum value in the 1950s and then fell. The 1960s are a period with small total forcing and the negative smoothed natural forcing due to two large tropical volcanic eruptions: Agung and Fernandina. Total natural and anthropogenic forcing reached a local maximum in the 1950s which according to our calculations was only exceeded towards the end of the 20th century.

⁴The tropopause was diagnosed using a simulation of HadAM3 forced with historical SSTs and ice (similar to that by *Rowell* [1998] using HadAM2b) for the period 1860–1997. The tropopause was diagnosed at every point and every radiation timestep, using the same lapse rate criteria used in The Met. Office operational forecast model, which are based on the WMO rules for reporting observations.

2.3 Observed datasets and data processing

We compare the results of the model simulations with an updated version of the surface temperature dataset of *Parker et al.* [1994] and with the HadRT2.1s radiosonde temperature dataset – an updated version of *Parker et al.* [1997]. Radiosonde data from the Indian subcontinent ($60^{\circ}\text{E} - 90^{\circ}\text{E}$, $0 - 30^{\circ}\text{N}$) was removed because of apparent problems with its quality and the remaining data corrected for known changes in instruments by comparison with co-located MSU data [*Parker et al.*, 1997].

Annual averages of both the surface and radiosonde datasets were computed from monthly-mean temperature anomalies. At each location we required there to be at least eight months of observations; otherwise we discarded the annual-mean value.

The annual-mean surface observations were decadal averaged, with periods ending in 1997. For each decade we required that there be at least 5 years of data; otherwise the decadal-mean value was discarded. In our analysis of surface temperature we consider changes on 50-year and 100-year timescales using decadal data with the 50-year or 100-year average removed. Locations in the observations at which less than three (five) decades were present were omitted in the 50 (100)-year analysis. This data was then filtered, using spherical harmonics, to remove scales below 5,000 km (T99, S00). Harmonics were further weighted by $1/\sqrt{2l+1}$ (l is the total spherical harmonic wavenumber) to give each spatial scale included equal weight [*Stott and Tett*, 1998]. Simulated data was decadal averaged, bilinearly interpolated in latitude and longitude to the observational grid. Simulated data was discarded where there were no observational data and then processed in the same way as the observations were.

When computing global-mean timeseries we first bilinearly interpolated (latitude and longitude) simulated annual-mean near-surface temperature data to the observational grid, discarding simulated data where there were no observational data. As the observed data are anomalies relative to 1961–90 we computed the 1961–90 climate mean for each simulation and the observations, removed it and computed global-means. In order to show changes relative to the beginning of the century we removed the global mean time-average for 1881–1920 from each timeseries.

Annual-mean simulated data from throughout the at-

mosphere was trilinearly (pressure, longitude and latitude) interpolated to the three-dimensional observed grid and discarded where there was no observed data. We then processed the simulations and observations by first removing the 1971–1990 mean, zonally averaging (requiring that there be four longitudes with data present in any zonal band) and then computing the difference between 1985–1995 and 1961–1980. Unlike T96 and AT99 simulated data had the observational mask applied and the 1971–90 normal removed before zonal averaging. This change in processing had little impact on the signals and tended to reduce slightly the variability of the annual-average zonal-mean temperatures [*Collins et al.*, 2000b].

Changes in surface temperature observed over the century show warming (Fig. 2(a)) over most of the world with, in general, land warming more than the ocean, central Eurasia and Canada warming most and cooling occurring in parts of the North Atlantic to the south of Greenland and Iceland.

The free atmosphere changes show cooling (Fig. 2(b)) in the stratosphere and warming in the troposphere. The cooling extends down to 500 hPa above the Arctic — far below the reanalysis tropopause. The tropospheric warming is uneven with a maximum warming of 0.6K occurring at about 50°N and almost no warming at 30°N . Differences between the observations shown here and that of T96 (see their Fig. 2D) are due to the continued development of the radiosonde dataset and removal of data from the Indian sub-continent.

3 Model and Observed Temperature Responses

Annual means of global-mean temperature from the ensemble averages (Fig. 3) show that the simulated responses are all inconsistent with the observations. From the 1920s until the 1950s GHG warms less than the observations. From the 1940s onwards it begins to warm and by the end of the 20th century has warmed more, over the century, than the observations. Addition of sulphates and ozone to GHG, giving ANTHRO, delays the simulated warming until the 1960s. From then till the end of the century ANTHRO, TROP-ANTHRO and the observations warm at approximately the same rate. The small differences between ANTHRO and TROP-ANTHRO suggest that stratospheric ozone changes have

little impact on near-surface temperature despite the large differences in radiative forcing (Fig. 1). We believe that this small response is due to the stratospheric ozone forcing being concentrated over Antarctica.

Natural forcings, in our simulations, produce a general warming from the 1910s, until the eruption of Agung in 1963. After this the observations warm while the subsequent eruptions of El Chichón and Pinatubo cool NATURAL.

The patterns of simulated response from the 20th century are shown in Fig. 4. All three anthropogenic ensembles (GHG, TROP-ANTHRO and ANTHRO) produce more warming over land than over the sea. GHG has the most warming of these ensembles and warms more than the observations. In the GHG ensemble the Arctic warms most while the North Atlantic and large regions of ocean in the southern hemisphere warm considerably less than the global average (Fig. 4(a)). ANTHRO and TROP-ANTHRO are in reasonable agreement with the observations (Fig. 2(a)), and both warm less than GHG especially in the mid-latitudes of the northern hemisphere where the sulphate cooling will be large. NATURAL shows no distinctive signal, probably because there is little change in natural forcing between the start and end of the century (Fig. 1).

We now examine temperature changes throughout the atmosphere between the decade 1985–1995 and the twenty year period 1961–1980. All three anthropogenic ensembles have similar warming in the troposphere, greatest warming in the upper tropical troposphere and warm more in the northern hemisphere than the southern (Fig. 5). The upper tropical troposphere and southern hemisphere warm more in GHG than in TROP-ANTHRO while high northern latitudes warm less. The latter could be due to the effects of tropospheric ozone or to internal climate variability. Neither simulation cools the stratosphere or upper troposphere as much as the observations (Fig. 2(b)). Inclusion of stratospheric ozone decline in ANTHRO produces large stratospheric cooling (of up to 6K over Antarctica), especially in high latitudes, which brings this ensemble into better agreement with the observations (Fig. 2(c)). Unlike the anthropogenic simulations NATURAL warms in the tropical stratosphere, probably due to the 1991 Pinatubo eruption, but has little temperature response in the troposphere.

The boundary between cooling and warming is close to the tropopause in all ensembles except over Antarctica in ANTHRO (Fig. 5). In this ensemble the cooling over Antarctica extends down to 500 hPa and the

tropopause rises, its pressure falling by 50 hPa. The data over Antarctica is insufficient to tell if this occurred in reality. However, the observed Arctic cooling down to 500 hPa is not present in any of the ensembles.

Qualitative comparison of our ensembles with the observations suggests that ANTHRO is the most similar to the observations (compare Fig 5(c) with Fig 2(b)). As all the anthropogenic ensembles are quite similar in the troposphere it appears that increases in greenhouse gases and stratospheric ozone decline are the most important contributors to temperature changes in the free atmosphere.

4 Detection and Attribution Methodology

One of the main problems in attributing climate change to possible causes arises from the difficulties in estimating the radiative forcing and climate response due to different forcings. In particular, there are large uncertainties in the overall magnitude of the climate response to a given forcing due, for example, to uncertainties in climate sensitivity or the rate of ocean heat uptake[Kattenberg *et al.*, 1996]. The size of the forcing associated with many of the factors other than well mixed greenhouse gases, notably aerosols, is also uncertain[Shine *et al.*, 1995]. To reduce the impact of these uncertainties, we use a methodology first proposed by Hasselmann [1979] which has been shown to be a form of multivariate regression (AT99). This assumes that the observations (\mathbf{y}) may be represented as a linear sum of simulated signals (\mathbf{X}) and internal climate variability (\mathbf{u}):

$$\mathbf{y} = \mathbf{X}\beta + \mathbf{u} \quad (1)$$

where β_i is the scaling factor, or amplitude, that we apply to the i^{th} signal (\mathbf{x}_i) to obtain the best fit to the observations. In this paper the signals are ensemble averages from the simulations described earlier. Any errors in the *magnitude* of the forcing and climate responses are allowed for through scaling the model responses (\mathbf{x}_i) by the signal amplitudes (β_i). Errors in the *patterns* of forcing and response are not taken into account by this procedure. The values of β which give the best fit (the best-estimate value $\tilde{\beta}$) to observations, using the standard linear regression approach are (AT99):

$$\tilde{\beta} = (\mathbf{X}^T \mathbf{C}_N^{-1} \mathbf{X})^{-1} \mathbf{X}^T \mathbf{C}_N^{-1} \mathbf{y} = \mathbf{F}^T \mathbf{y} \quad (2)$$

where C_N is the covariance matrix of natural variability ($\mathcal{E}(\mathbf{u}\mathbf{u}^T)$) estimated, in our case, from simulations of coupled-atmosphere ocean GCMs. We do not normally have enough data to accurately estimate the inverse covariance matrix (C_N^{-1}) so we estimate its inverse from a truncated representation of it based on its leading eigenvectors. Simulated and observed data are also filtered by projection onto these eigenvectors.

Both the observations and signals include internal climate variability (noise) which leads to uncertainty in $\tilde{\beta}$. We estimate uncertainty ranges (the 5–95% range unless stated otherwise) in $\tilde{\beta}$ using its covariance matrix (AT99 and Mardia *et al.* [1979]):

$$\tilde{V}(\tilde{\beta}) = F^T C_{N_2} F, \quad (3)$$

where C_{N_2} is an estimate of $\mathcal{E}(\mathbf{u}\mathbf{u}^T)$ using data which is statistically independent of that used to estimate C_N .

We perform two related tests:

detection This tests the null-hypothesis that the observed response to a particular forcing or combination of forcings is zero. We do this by computing the two-tailed uncertainty range about $\tilde{\beta}$ using $\tilde{V}(\tilde{\beta})$ and testing whether it includes zero. Rejection of this null and a positive value of $\tilde{\beta}_i$ implies detection.

amplitude-consistency This tests the null-hypothesis that the amplitude of the observed response is consistent with the amplitude of the simulated response. We do this by computing the two-tailed uncertainty range about $\tilde{\beta}$ using $\tilde{V}(\tilde{\beta})$ and testing whether it includes unity. In this test we inflate $\tilde{V}(\tilde{\beta})_{ij}$ by a factor of $\sqrt{(1 + 1/m_i)}\sqrt{(1 + 1/m_j)}$ to compensate for sampling noise in the signals, where m_i and m_j are the ensemble sizes. Failure of this test means that the simulated signal amplitude is inconsistent with the observations. When we report consistency with unity, we mean that it is neither greater than nor less than unity at a given confidence level.

Unless otherwise stated, results are reported as significant if the relevant null-hypothesis can be rejected at the 5% level. All reported uncertainty ranges are 5–95%.

The best estimate of the temperature trend (or any other linear diagnostic such as change in global-mean temperature), due to a forcing factor, is the product of the signal amplitude and the trend computed from

the appropriate ensemble-average. The covariance matrix used to compute uncertainties is computed by multiplying $\tilde{V}(\tilde{\beta})_{ij}$, inflated by $\sqrt{(1 + 1/m_i)}\sqrt{(1 + 1/m_j)}$ to approximately compensate for signal-noise, by the trends of the i^{th} and j^{th} ensembles.

Covariance matrices are estimated from intra-ensemble variability (i.e. variability within the ensemble) and from CONTROL. To obtain these estimates we process data in exactly the same manner as we do the observations and simulations giving the \mathbf{u} in eqn. (1). In all our analyses realisations of \mathbf{u} were overlapped by ten years. When computing covariance matrices from intra-ensemble variance we remove the ensemble average and scale each realisation by a factor of $\sqrt{(m - 1)/m}$ where m is the number of ensemble members.

In Section 5 we analyse changes in near-surface temperature on 100-year timescales (century) and on 50-year timescales (50-year), and changes in zonal-mean temperature throughout the atmosphere (free-atmosphere). The two near-surface analyses examine changes in time and in space while the free-atmosphere analysis looks at spatial changes over a thirty-five year period (Section 2.3).

For both the 50-year and the free-atmosphere analysis we use intra-ensemble variability from the GHG, ANTHRO and NATURAL ensembles to estimate C_N and data from CONTROL to estimate C_{N_2} . Any significant differences between C_N and C_{N_2} would reduce the power of the optimisation algorithm (i.e. increase uncertainty ranges) but would not introduce a bias in the estimated signal amplitudes.

For the century analysis we believe that nine realisations of century timescale variability from the intra-ensemble variability of HadCM3 is not enough to generate a sufficiently reliable estimate of C_N . Therefore we use control and intra-ensemble variability from five ensembles of HadCM2 (S00) to estimate C_N while C_{N_2} is estimated using HadCM3 CONTROL and intra-ensemble variability from the GHG, ANTHRO and NATURAL ensembles.

4.1 Consistency

We test that the best-estimate combination of signals is consistent with our linear statistical model (Eqn 1) by computing the residual sum of squares:

$$R^2 = \sum_{i=1}^{\kappa} \frac{(y_i - \sum_{j=1}^n X_{ij}\tilde{\beta}_j)^2}{C_{N_2 ii}}. \quad (4)$$

where i is an index over the ranked eigenvectors of C_N , j is an index over signals and κ is the number of eigenvectors used to filter signals and observations (see subsection 4.3 for details).

In the case of noise-free signals R^2 has a distribution that lies between $(\chi^2(\kappa - n))/\kappa$ and $F(\kappa - n, \nu_2)$ where ν_2 is the dof of C_{N_2} . We use the F distribution at the 90%, rather than the 95%, level to test for consistency. As an *ad hoc* correction for noise in the signals we scale R^2 by $1/(1 + s)$, and assume that it still has the same distribution, where s is:

$$s = \sum_{i=1}^n (\tilde{\beta}_i / m_i)^2$$

and m_i is the number of ensemble members in the i^{th} ensemble. The justification for this *ad hoc* scaling is that the expected difference between the observations and the best-estimate response would be larger by a factor of $\sqrt{1 + s}$ due to the noise in the simulations. In the case of signals (and observations) with high signal-to-noise ratio we verified this scaling by Monte-Carlo tests.

4.2 Estimated degrees of freedom for covariance matrices

In order to compute uncertainties and truncations we need an estimate of the degrees of freedom (dof) of the covariance matrices we compute. These matrices are computed from various different datasets and their dof is the sum of the dof of the individual datasets. For CONTROL the estimated dof, assuming maximally overlapped data, is the number of non-overlapping realisations multiplied by 1.5 (Allen and Smith [1996]; S00) and rounded down to the nearest integer. For each ensemble the estimated dof is the number of non-overlapping segments in a single simulation multiplied, again, by 1.5, rounded down to the nearest integer and then multiplied by $m - 1$ (to account for removal of the mean).

The estimated dof for the two covariance matrices used in our analysis are shown in Table 1. Note that the estimated dof of $\tilde{V}(\tilde{\beta})$ is that of C_{N_2} .

The estimated degrees of freedom for the century analysis (see Table 1) may be over-optimistic as the individual HadCM2 ensemble members were all initialised from the same 1700-year control. Furthermore the last three simulations of each of the two solar ensembles were initialised by applying small random per-

turbations to the first solar simulation in each ensemble. Similarly the three HadCM3 ensembles were all initialised from the same HadCM3 control. 100-year segments may not be completely independent of one another. Uncertainty in the dof of C_{N_2} is relatively unimportant: halving the dof used in our statistical tests increases the uncertainty ranges by 4%. The estimated dof of C_N is used to determine the maximum allowable truncation (see below) and so we explore the sensitivity of our results to truncation.

4.3 Truncation

If C_N is an order $n \times n$ matrix, then where possible, we perform all analysis at the smaller of its dof and n . If the consistency test all further analysis is carried out at this truncation (κ). All data is then filtered by projection onto the leading κ eigenvectors of C_N . If the test fails at this truncation then we carry out the analysis at the largest truncation at which the test passes and explore the reasons for the test failure.

Our estimated dof are somewhat arbitrary as are the criteria we use to determine truncation. Therefore we explore the sensitivity of our results to truncation.

4.4 Degeneracy

We used the same three empirical tests as T99 and S00 to test for signal degeneracy or co-linearity (see pages 243–248 of Mardia *et al.* [1979]). These three tests give empirical estimates of the number of independent “factors” in the signal combination. We conclude that a signal combination is likely to be degenerate if the maximum value of those three tests is less than the number of signals being considered.

If two signals are degenerate, the usual consequence is that uncertainty ranges are large. Then there are likely amplitudes far from the best-estimate amplitudes. It is also likely that neither signal is individually detectable, since a range of linear combinations are equally consistent with the data including those which assign zero amplitude to one signal or the other. However, specific combinations of these signals may easily be detectable and have smaller uncertainty ranges.

4.5 Transformations

We assume that the three anthropogenic signals (GHG, ANTHRO and TROP-ANTHRO) are linear combinations of the following physically-based signals:

- G** Response to well-mixed greenhouse gases alone.
- O_T** Response to stratospheric ozone changes.
- O_S** Response to stratospheric ozone decline.
- O** Response to both stratospheric and tropospheric ozone changes.
- S** Response to sulphates (indirect and direct)

namely,

$$\begin{aligned}
 \text{GHG} &= G \\
 \text{ANTHRO} &= G + S + O = GSO \\
 \text{TROP-ANTHRO} &= G + S + O_T = GSO_T.
 \end{aligned}$$

The amplitudes and covariance matrices of these physically based signals are given by a linear transformation of the original amplitudes and of $\tilde{V}(\tilde{\beta})$ – see Appendix C for details. For example, suppose we model the observations as a linear superposition of the GHG and ANTHRO simulations:

$$\mathbf{y} = \mathbf{x}_{\text{GHG}}\tilde{\beta}_{\text{GHG}} + \mathbf{x}_{\text{ANTHRO}}\tilde{\beta}_{\text{ANTHRO}}.$$

$\tilde{\beta}_{\text{GHG}}$ in this equation is not simply the estimated amplitude of the greenhouse response. It is the *additional* greenhouse response we need to add to the best-fit ANTHRO simulation to obtain the best overall fit to the observations. In this case the amplitude of the greenhouse and “other anthropogenic” signals is:

$$\begin{aligned}
 \tilde{\beta}_G &= \tilde{\beta}_{\text{ANTHRO}} + \tilde{\beta}_{\text{GHG}} \\
 \tilde{\beta}_{SO} &= \tilde{\beta}_{\text{ANTHRO}}.
 \end{aligned}$$

In this example, the variance in $\tilde{\beta}_G$ is equal to the sum of the variances in $\tilde{\beta}_{\text{GHG}}$ and $\tilde{\beta}_{\text{ANTHRO}}$.

4.6 Signal-to-noise

Amplitude uncertainty ranges, and particularly the upper bound, estimated from signals with a low signal-to-noise ratio are likely to be incorrect[Allen and Stott, 2000]. We use the following summary statistic for the j^{th} signal to give us some guidance when this may be occurring:

$$(\text{SNR})^2 = \frac{m_j}{\kappa} \sum_{i=1}^{\kappa} \frac{X_{ij}^2}{C_{N_2 ii}}$$

where κ is the truncation. When the “signal” \mathbf{x}_j is pure Gaussian noise $(\text{SNR})^2$ has an expected value of 1 and is distributed similarly to R^2 of Section 4.1 (between $(\chi^2(\kappa))/\kappa$ and $F(\kappa, \nu_2)$). We use a F-test at the 90% level to determine if there is significant noise contamination.

5 Detection and Attribution of Observed Temperature Changes

5.1 Changes in near-surface temperature on century timescales

We now examine changes in near-surface temperature from 1897–1997 using both spatial and temporal information. For most of the 20th century TROP-ANTHRO and ANTHRO are identical and therefore we use the latter in subsequent analyses. We transform the amplitudes of GHG and ANTHRO to obtain amplitudes of G (greenhouse gases) and SO (sulphates and ozone) as described in Section 4 and Appendix C. Tests for degeneracy suggest that we can reliably estimate the amplitude of G , SO and NATURAL signals simultaneously (Table 1). Thus all further analysis is done using this combination of signals.

The filtered observations (see Section 4) contain more than 96% of the observed variance (Table 1) and the residuals are consistent with those expected from CONTROL (Fig. 6(a)) at all truncations. All three signals are detected (Fig. 7 left) demonstrating that all have had a significant impact on changes in near-surface temperature over the 20th century. Furthermore, the amplitudes are all consistent with unity—the model is consistent with observations on decadal timescales and on continental to global spatial scales.

Signal-to-noise ratio is large for the anthropogenic signals but small for NATURAL (Table 1) suggesting it is significantly noise-contaminated. Though our detection of NATURAL is probably robust, its estimated amplitude ranges, and in particular the upper range, are sensitive to this noise contamination[Allen and Stott, 2000].

We reconstruct the global-mean temperature changes from the best-estimate signal amplitudes and simulated responses (Fig. 8). Well-mixed greenhouse gases and other anthropogenic effects (largely the indirect effect of sulphate aerosols) almost balance giving a total anthropogenic warming of approximately 0.1K from the beginning of the 20th century to the 1960s. There-

after anthropogenic effects warm the planet by approximately 0.5K. From the 1950s onwards natural and anthropogenic non-greenhouse gas forcings each cause a cooling of about 0.1K. Together they offset about 0.2K of the estimated 0.6K warming due to greenhouse gases over the same period.

While Fig. 8 shows the best-estimate combination of signals, it is even more important to consider uncertainty ranges. These are most easily summarised in terms of linear trends (Fig. 9) over selected periods (the entire century, 1897-1947 and 1947-1997 – see Section 4 for details.) Over the 20th century anthropogenic forcings cause a warming trend of 0.5 ± 0.15 K/century. The trend due to greenhouse gases is 0.9 ± 0.24 K/century while the remaining anthropogenic factors cool at a rate of 0.4 ± 0.26 K/century. Over the century natural forcings contribute little to the observed trend.

During the early century greenhouse gases and natural forcings cause warming trends of about 0.2 to 0.3 K/century while other anthropogenic factors produce negligible cooling trends (Fig. 9). Over the last half of the century greenhouse gases warm the climate at a rate of 1.7 ± 0.43 K/century with natural forcings (largely volcanic aerosol) and other anthropogenic factors (mainly the indirect effect of sulphate aerosols) both causing an estimated cooling trend of about 0.3 ± 0.2 K/century. Thus, since 1947 changes in aerosol concentrations (anthropogenic and natural) have offset at least a third of the greenhouse gas warming.

The uncertainties in the signal amplitudes are correlated due to internal climate variability in both the observations and the signals. The joint confidence regions allows us to examine how uncertainty in one amplitude affects the uncertainty in another. We find that all three simulated signals are simultaneously consistent with the observations (i.e. the point (1,1,1) is within the three-dimensional uncertainty ellipsoid) as are any combination of two signals (i.e. all the solid ellipses in Fig. 10 include the point (1,1)). The uncertainty ellipse for the two anthropogenic signals has a strong tilt showing that these signals are highly correlated. Thus large values of G are consistent with large values of SO i.e. the observations require a larger greenhouse gas warming to accompany a stronger cooling from sulphates. Over the century there is little tilt between the natural and either of the anthropogenic signals. Thus errors in the amplitude of the natural signal have little impact on the estimated amplitude of the two anthro-

pogenic signals. Consequently the uncertainties in the linear trends (Fig. 9) due to NATURAL are independent from those due to SO and G .

One “technical” issue in optimal detection is the eigenvector truncation used. Our results are insensitive to truncation for both detection (the light grey inner regions in the top row of Fig. 11 do not include zero) and “amplitude-consistency” (the black outer regions include one).

If we omit the effect of stratospheric ozone decline, by replacing ANTHRO with TROP-ANTHRO, we find little change in the residuals and only small changes in the amplitudes. Elimination of stratospheric ozone depletion causes a slight reduction in the cooling attributed to other anthropogenic effects from 1947 onwards which, in this analysis, is compensated for by a small increase in cooling due to natural forcings.

5.2 Sensitivity to processing and variability estimates

In this subsection we explore the sensitivity of results from the previous analysis to details of the data-processing and to increases in the magnitude of the simulated climate variability. We consider the following cases:

No-weight Here we did not apply the weighting of $1/\sqrt{2l+1}$ to the spherical harmonics.

Index Rather than projecting simulated and observed data onto spherical harmonics three indices were computed – the global average, the land temperature and the northern-hemisphere minus the southern-hemisphere.

90-year Rather than doing the analysis for the century we carried out the analysis on two 90-year segments (1897–1987 and 1907–97).

In the 90-year 1907–97 and Index sensitivity studies we find that the simulations and observations are inconsistent (Section 4.1) at the largest truncations we consider (Fig. 6(b)). Therefore we truncate at the largest truncation that are consistent with the observations (Table 1). We carry out both 90-year analyses at the truncation determined by the 1907–97 case.

We repeat these analyses and the century case at half the largest truncation to see if our results are insensitive to truncation. Thus, including the “normal” data-processing at truncation 20, we examine a total of nine

sensitivity studies giving ten cases in all. At these truncations the filtered observations contain at least 80% of the observed variance (Table 1), except in two cases.

The SNR for the anthropogenic signals is always larger than two suggesting little noise contamination (Table 1). By contrast, SNR for NATURAL is close to one and in half the cases is not significantly different from that expected by chance. There is evidence of signal co-linearity (see Section 4.4) in three cases (Table 2) meaning that results in those cases may be sensitive to small changes in the signals. We find:

- G is detected in all cases (Table 2).
- SO is detected in all but two cases, both at half the maximum truncation.
- NATURAL is detected in all but two cases.

All amplitudes are consistent with unity (Table 2). Therefore we conclude that our detection and amplitude-consistency results are robust to changes in both processing and truncation. The best-estimate amplitudes are, however, more sensitive to these choices with $\tilde{\beta}_{\text{NATURAL}}$ extending from 0.60 to 1.11, $\tilde{\beta}_G$ varying from 0.77 to 1.03 and $\tilde{\beta}_{SO}$ ranging from 0.49 to 0.89 (Table 2).

Our claims of signal detection all rely on simulated internal climate variability. We compute how much the model variability need be increased to prevent the detection of the signals all the cases considered above. The simulated variability needs to be inflated by 2.2 to 4.4 to nullify our detection of greenhouse gases (Table 3) (an increase in variance of 5 to 19). However, detection of the GS and NATURAL signals is much less robust. Here an increase in variability by 40% (i.e. an increase in variance of 2) is enough to stop detection of GS and NATURAL in half the cases considered.

5.3 Surface temperature changes on 50-year timescales

We now examine changes on 50-year timescales to allow comparison with the HadCM2 results of T99 and S00. Six 50-year periods, each of five decadal means, are considered: 1897–1947, 1907–57, . . . , 1947–97. At least 85% of the observed variance (Table 1) is captured in these periods. Unlike the century analysis the signals are generally not significantly noise contaminated (Table 1), though the signal-to-noise ratio is below 1.5 for NATURAL and ANTHRO before 1937. We

use the same signal combination ($G SO$ NATURAL) as used in the century analysis and find evidence of signal degeneracy during 1927–77 and 1937–87 (Table 1). The residuals are consistent with the variance computed from CONTROL at almost all truncations and all periods (Fig. 6(c)).

The effects of well-mixed greenhouse gases and other anthropogenic effects are detected in all six 50-year periods with amplitudes always consistent with unity (Fig. 7). Natural effects on climate are only detected during the 1907–57 period (Fig. 7) whereas the amplitudes are consistent with unity only in 1897–47, 1907–57, and 1927–77.

In the two periods of significant climate change (1907–57 and 1947–97) we consider how robust our results are to changes in truncation. Detection of both the anthropogenic signals during these periods, unlike the natural signal, is largely robust to truncation (Fig. 11). All signal-amplitudes are consistent with unity except during 1947–97 for NATURAL at all truncations and G for truncations below 13.

Best-estimate global-mean temperature changes and trends (Section 4) are proportional to the amplitudes shown in Fig. 7. Thus we can compare best-estimate changes and trends from the 50-year and century analyses by comparing their amplitudes. The 50-year analyses produce smaller natural changes than the century analysis except in the 1907–57 period. Cooling from sulphates and ozone is about the same in both cases while greenhouse gas warming is less in the 50-year analyses from 1927 onwards (Fig. 7). Thus total anthropogenic changes and trends are generally smaller in the 50-year analyses than in the century analysis.

Only in the 1907–57 analysis do natural forcings make a substantial contribution to temperature trends (Fig 12). Furthermore the the temperature trend due to anthropogenic forcings is close to zero. In this period amplitudes, and hence temperature trends, of all three signals are also very similar to the century analysis (Fig. 7).

In the 1907–57 analysis the difference between the best estimate and the observed trend (residual) is largest of all the periods considered (Fig. 12). The residual is still consistent with our estimated internal climate variability and so could be due to internal climate variability alone. It could also be, partly or wholly, due to observational error, error in the forcing timeseries, some other forcing not considered in our analyses, model error or noise in the signals. T99 found a large residual in their $GS SOL$ analysis (see Fig 2(b) of T99) in the

1906–1956 period suggesting that this result is robust to using the solar timeseries of *Hoyt and Schatten* [1993], neglecting the effect of volcanos and use of a different model. *Hegerl et al.* [2000a] found that observational error was much smaller than internal variability. This suggests that the large residual is probably due to internal climate variability.

Thus the 1907–57 warming is best explained by a combination of natural forcings (an increase in solar irradiance, a lack of large volcanic forcing and a recovery from earlier volcanic forcing), near-zero response to total anthropogenic forcing *and* a large warming from internal climate variability. If correct this suggests that a large part of the early century warming is due to a combination of natural forcing and natural internal variability. In other words it is naturally caused. In our simulations “sulphates” offset most of the greenhouse warming prior to the 1960s. If this were not the case then we would be likely to have smaller residuals and thus estimate a smaller contribution from internal climate variability to the early century warming.

The model is consistent with the observations in the two 50-year periods of significant climate change (1907–57 and 1947–97). In these periods the uncertainty ellipses for the two anthropogenic signals are strongly tilted showing that these signals are highly correlated (Fig. 10). The natural and anthropogenic signals are less correlated. In 1947–97 the tilt is such that a larger amplitude of the G signal requires a larger amplitude of the NATURAL signal, whereas the ellipse is weakly tilted in the opposite direction in the 1907–57 period. The natural and anthropogenic signals are less correlated in the century analysis than in either of the 50-year analyses. Therefore the former analysis is better at discriminating between natural and anthropogenic forcings than the latter. All three signals are simultaneously consistent with the observations (the point $(1, 1, 1)$ is inside the three dimensional ellipsoid centred on $\hat{\beta}$) in all periods except 1917–67.

We can compare our results with those of T99 and S00 though our experimental design differ from theirs. For example we included the effects of ozone while they did not. Unlike T99 and S00 we detect anthropogenic influences in all 50-year periods considered. Our detection of a combined solar and volcanic effect on climate during 1907–57 corresponds to their detection of a solar influence during 1906–56. There are differences in the warming during this period (compare Fig. 13(a)) with Fig. 1(b) of T99), some of which may be due to use of the solar forcing of *Lean et al.* [1995a] rather

than that of *Hoyt and Schatten* [1993]. The total anthropogenic changes for 1947–97 are similar to those of T99. However our analysis has less “sulphate” cooling and greenhouse warming than T99 – compare Fig. 13(b) with Fig. 1(c) of T99.

The linear trend and uncertainty range for each signal are comparable with those computed by T99 (compare Fig. 2 of T99 with Fig. 12). As in T99 the total anthropogenic warming trend is only greatly different from zero in the 1947–97 period. There is more greenhouse warming and sulphate cooling in our analysis than in T99 (compare Fig. 12 with Fig. 2(a) of T99) in all but the 47–97 period. Thus, while the total anthropogenic warming estimate here (using HadCM3) is similar to that of T99 and S00 (using HadCM2) the partitioning into warming from greenhouse gases and cooling from other anthropogenic forcings is different.

Finally, as in the earlier century analyses we omit the effect of stratospheric ozone decline and repeat our analysis. We find that the residuals are similar except during 1947–97 when the fit to observations is too good for truncations greater than 17. Though the same signals are detected, the amplitude of G is significantly smaller than unity in the 37–87 and 47–97 analyses meaning that the simulated response is incorrect. We also find that anthropogenic aerosols and tropospheric ozone offset less greenhouse warming in 1947–97 than our original 50-year analysis. As the near-surface temperature responses in ANTHRO and TROP-ANTHRO are similar then some of our results may be sensitive to noise contamination. Alternatively they may be sensitive to the highly uncertain ozone forcing.

5.4 Free atmosphere changes

We now examine the difference between the 10-year zonal-mean from 1986–1995 and the 20-year zonal-mean for 1961–1980 as in AT99.

Earlier we showed that the changes in the free atmosphere simulated by TROP-ANTHRO and GHG are similar. We therefore do not use GHG in this analysis, examining combinations of TROP-ANTHRO, ANTHRO and NATURAL. This assumes that the relative amplitudes of the G and SO_T responses are as in TROP-ANTHRO. To separate the impact of stratospheric ozone decline from all other anthropogenic effects we transform the amplitude of the TROP-ANTHRO and ANTHRO signals to give amplitudes of GSO_T (all anthropogenic forcings except stratospheric ozone decline) and O_S (stratospheric ozone decline on climate)—see

subsection 4.5 and Appendix C for details.

In the three-signal case the maximum truncation of C_N is seven. For truncations beyond this the ratio of the residual to control variance is three to five times too large (Fig. 14(a)). At truncation seven the filtered observations contain 48% of the observed mass-weighted variance (Table 1) compared to 71% at truncation 36 (the truncation we believe the largest we can reasonably consider given the estimated dof of C_N — Table 1).

The SNR for the two anthropogenic signals is reasonably high (Table 1), while the SNR for the natural signal is less than one.

The GSO_T O_S and NATURAL case has residual variance consistent with CONTROL for all truncations less than or equal to seven (Fig. 14(a)). Detection of GSO_T , but not of O_S or NATURAL, occurs at those truncations (Fig. 14(b)). While the amplitudes of O_S and NATURAL are consistent with unity the same is not true of GSO_T which has a best-estimate value of 0.65. This suggests that the simulated tropospheric response is about 50% stronger than the observed response.

Failure to detect NATURAL does not rule out the possibility of a significant natural influence on climate. The simulated signal is weak and noise contaminated and so our failure to detect it does not strongly rule out the possibility of some process which preferentially amplifies the response to solar or volcanic forcing. Furthermore there remains the possibility that natural effects may have an influence on shorter timescales. For example the stratospheric warming associated with volcanoes and possible links between changes in the upper tropospheric circulation and the solar cycle e.g. *Salby and Callaghan* [2000]; *Hill et al.* [2000].

Above truncation seven the residual variance is approximately three to five times larger than that of CONTROL (Fig. 14(a)) and we now consider why this might be. The observations filtered by these leading seven eigenvectors do capture the gross features of the tropospheric warming (Fig. 15(a)). However, at this truncation, the filtered observations do not show the observed stratospheric cooling (Fig. 2(b)) as seen more clearly in the difference between the raw and the filtered observations (Fig. 15(b)). The raw observations are cooler in the stratosphere and approximately 0.1K warmer throughout large regions of the troposphere than the filtered observations. Therefore our failure at truncations greater than seven is probably due to the simulated stratospheric variability being too small though gross signal error cannot be ruled out. At truncation seven

the best-estimate warming from GSO_T is similar to the filtered observations (Fig. 15(a)) in the troposphere.

6 Summary and Conclusions

We have presented results from a set of simulations of HadCM3. It has a physically based interactive sulphur cycle, a simple parametrisation of the first indirect effect of sulphate aerosols [*Twomey*, 1974] and a better radiation scheme than its predecessor, HadCM2, allowing explicit representation of well-mixed greenhouse gases. HadCM3 has higher resolution in the ocean than HadCM2 and additional changes were made to the atmospheric component of the model. These changes have removed the need for flux adjustments to keep the model stable for multi-century integrations

We forced the model with “historical” changes in greenhouse gas concentrations, sulphate emissions, tropospheric and stratospheric ozone, solar irradiance changes and changes in volcanic stratospheric aerosol in four ensembles each of four simulations. Total simulated anthropogenic forcing is almost constant from 1980 onwards due to a strong negative forcing from stratospheric ozone decline. Despite this, ensembles with and without ozone decline warm at similar rates. This negative forcing due to ozone is outside the range quoted by *Schimel et al.* [1995] and is partly due to changes in tropopause height. Therefore, we plan to investigate both forcing and response in more detail in a subsequent publication. Other anthropogenic forcings are within the range quoted by *Shine et al.* [1995].

We found that the effects of well-mixed greenhouse gases, other anthropogenic effects (largely the indirect effect of sulphate aerosols), and natural causes (solar irradiance changes and volcanic eruptions) could be detected in the record of surface temperature change during the entire 20th century. The best-fit combination of simulations was consistent with observations during the century and in all 50-year periods we considered. We detected both anthropogenic signals in all six 50-year periods we investigated. We also detected the response to natural forcings in the 1907–57 period but this was not robust to some technical details of the analysis.

We found that the early 20th century warming can be explained by a response to natural forcings, a large warming, relative to other factors, from internal climate variability with the effect of greenhouse gases largely being balanced by other anthropogenic forcings. During 1907–57 we found that there was negligible net

anthropogenic warming with the effect of greenhouse gases largely being balanced by other anthropogenic forcings. Therefore, in this period, the warming was largely naturally caused. Reconstructions of temperature changes, using proxy indicators, of the last 500 to 1000 years [Crowley, 2000; Mann *et al.*, 1998] suggest that the observed warming in this period is unusually rapid. If our analyses are correct, in attributing it largely to natural causes, this was an unusual natural event. We believe that further investigation of this period is needed.

The late century warming was largely explained by greenhouse gases offset by the effect of volcanic aerosol and the indirect effect of anthropogenic aerosols. Over the entire century natural forcings make no net contribution as they warm early in the century and cool from the 1960s on. Greenhouse gases warm at a rate of 0.9 ± 0.24 K/century while other anthropogenic forcings cool at a rate of 0.4 ± 0.26 K/century giving a total anthropogenic warming of 0.5 ± 0.15 K/century.

On 50-year timescales our results are generally similar to that of Tett *et al.* [1999] with similar total anthropogenic warming. We find more warming from greenhouse gases and cooling from sulphates and ozone than Tett *et al.* [1999] in all periods except the 47–97 period, when we find less sulphate cooling. Thus the total anthropogenic warming is robust to using HadCM3 rather than HadCM2 but the contributions from different factors are less so.

We detected the effect of other anthropogenic forcings on the radiosonde record of temperature change in the free atmosphere from 1961–95 but with a simulated tropospheric response about 50% too large. We found no evidence of a climatic effect from stratospheric ozone decline nor a natural effect on the free troposphere. Analysis on shorter timescales might detect the influence of volcanic eruptions and the solar cycle.

The most crucial caveat in our work is that the variability we use to compute uncertainty limits is derived from simulations. Analysis of the free atmosphere suggests that the simulated stratospheric variance is too small by as much as a factor of five. Collins *et al.* [2000a] compared the variability of simulated summer near-surface temperatures from CONTROL with a proxy temperature dataset from circa 1400 to 1950. These results suggest that the internal variance of HadCM3 is two to three times smaller than the variance estimated from the proxy data but at least some of the differences may be due to neglect of naturally

forced climate variability. After inflating the simulated variance by a factor of five we still detected the effect of greenhouse gases though not other factors.

Before 1979 there is little direct measurement of the changes in solar irradiance and thus considerable uncertainty in its timeseries. For example we could have used the timeseries of Hoyt and Schatten [1993] rather than Lean *et al.* [1995a]. There is also some uncertainty in the forcing from explosive volcanic eruptions. Lacis *et al.* [1992] quote a forcing from volcanoes of 30 W/m^2 (without stratospheric adjustment) per unit aerosol optical depth. We find a forcing of 20 W/m^2 per unit aerosol optical depth once we include stratospheric adjustment. In the century analysis we found no evidence that the model's response to natural forcings was incorrect but found several 50-year periods when it was. As we only carried out simulations with total natural forcing we were not able to explore differential error in the solar and volcanic forcings.

European surface observations indicate that the model has about half the anthropogenic sulphate aerosol concentrations observed. Non-sulphate aerosols such as black carbon have not been taken into account. Since black carbon exerts a positive forcing and there should be a strong correlation between the spatial and temporal distributions of sulphur and black carbon emissions from fossil fuel combustion, this may mitigate the effect of the underestimated direct sulphate forcing. Furthermore, the bulk of the negative radiative forcing (offsetting the effect of the well-mixed greenhouse gases) is due to the first indirect effect of sulphate aerosol on cloud albedo, the magnitude of which is extremely uncertain [Schimel *et al.*, 1995] as is the impact of underestimating anthropogenic sulphate aerosol concentrations on it. We have not included the second indirect effect which increases cloud lifetime [Albrecht, 1989] which could be of similar importance to the first indirect effect.

In our simulations stratospheric ozone decline produced a strong negative forcing but a weak near-surface temperature response. If we neglect this forcing we find that the simulated response to greenhouse gases is significantly overestimated in the 1937–87 and 47–97 periods.

We have not considered the effects of other forcings such as changes in land-surface properties and mineral dust which could have effected climate. Nor have we considered the effect of observational error on our results which may be significant for the radiosonde data [Gaffen *et al.*, 2000]. Finally we have not explicitly

considered the effect of noise in the signals. In the century analysis the natural signal has a low signal-to-noise ratio so that its estimated amplitude is biased towards zero and the computed uncertainty ranges are probably too small. Work is in progress to investigate the effects of such contamination. Nevertheless our results strongly suggest that anthropogenic forcings have been the dominant cause of temperature changes over the last 30 to 50 years.

Acknowledgments

Financial support to carry out the simulations and fund SFBT, PAS, GSJ, DCH, AJ, CEJ, DLR, DMHS and MJW was provided by U.K. Dept. of Environment Transport and the Regions contract PECD 7/12/37. JFBM, WJI and TCJ were all supported by the U.K. Public Met. Service Research contract. MRA was supported by a Research Fellowship from the U.K. Natural Environment Research Council. Supplementary support was provided by European Commission contract ENV4-CT97-0501 (QUARCC). The help and encouragement of Geoff Jenkins during the work reported here is gratefully acknowledged as is the contribution of the many colleagues who developed HadCM3.

Appendix A Notation

$\tilde{\beta}$	Best-estimate scaling of simulated signals.
C_N	Covariance matrix used for optimisation.
C_{N_2}	Covariance matrix used to estimate uncertainties.
ν_1	Estimated dof of C_N .
ν_2	Estimated dof of C_{N_2} .
X	Matrix of simulated signals. Each column is a signal.
y	Observations.
$\tilde{V}(\tilde{\beta})$	Covariance of $\tilde{\beta}$.
κ	Truncation applied to C_N .
m_i	Size of i^{th} ensemble.
GHG	Simulated response to well-mixed greenhouse gases.
ANTHRO	Simulated response to greenhouse gases, sulphates and ozone.
TROP-ANTHRO	As ANTHRO but without stratospheric ozone decline.
NATURAL	Simulated response to natural forcings.
CONTROL	Control simulation.
G	Response to well-mixed greenhouse gases.
S	Response to direct and first indirect effect of sulphates.
O_T	Response to tropospheric ozone
O_S	Response to stratospheric decline.
O	Response to changes in stratospheric and tropospheric ozone.
GSO_T	Combined response to changes in well-mixed greenhouse gases, sulphates and tropospheric ozone.
SO	Combined response to changes in sulphates and ozone.
SO_T	Combined response to changes in sulphates and tropospheric ozone.

Appendix B Computations of Radiative Forcings

Radiative forcing at the tropopause varies due to changes in the composition of radiatively active substances such as CO_2 and aerosols and also in the climate of the stratosphere[Schimel *et al.*, 1995; Hansen *et al.*, 1997]. In this appendix we derive an expression that allows us to calculate it and then show how the forcing was computed for each component.

Radiative forcing (ΔF) is defined as:

$$\Delta F = F(S_1, R_1) - F(S_0, R_0) \quad (5)$$

where F is the net flux across the tropopause, S is the stratospheric climate and R is the composition of the radiatively active substances. States are labelled 1 (perturbed state e.g. current concentrations of CH_4) and 0 (reference state against which forcing is computed e.g. pre-industrial concentrations of CH_4).

We can rewrite Eqn. (5) as:

$$\Delta F = \Delta_S F(R_0) + \Delta_R F(S_1) \quad (6)$$

where we define:

$$\Delta_S F(R_0) = F(S_1, R_0) - F(S_0, R_0)$$

and

$$\Delta_R F(S_1) = F(S_1, R_1) - F(S_1, R_0)$$

From the perturbed simulations we diagnosed the instantaneous forcing ($\Delta_R F(S_1)$) by calling the radiation scheme twice. In one call the changes in forcing agents were applied (R_1), and in the other the forcing agent was kept at its pre-industrial composition (R_0). After both calls the increments from the first call were then applied to update the model state with radiative diagnostics stored from both. The instantaneous forcing was then computed as the difference in total flux at the tropopause (diagnosed by the model at each point and timestep) between the two calls. This differs from *Schimmel et al.* [1995] who compute instantaneous forcing from $\Delta_R F(S_0)$.

We computed the adjustment of the forcing ($\Delta_S F(R_0)$) as the change in downward flux ($\Delta_S F^\downarrow(R_0)$) at the tropopause with any change in the upward flux being considered part of the climate system's response, not its forcing. Then we have:

$$\begin{aligned} \Delta_S F^\downarrow(R_0) &= F^\downarrow(S_1, R_0) - F^\downarrow(S_0, R_0) \\ &= F^\downarrow(S_1, R_1) - \Delta_R F^\downarrow(S_1) - F^\downarrow(S_0, R_0) \end{aligned}$$

This then gives the total radiative forcing:

$$\Delta F = \overbrace{F^\downarrow(S_1, R_1) - \Delta_R F^\downarrow(S_1) - F^\downarrow(S_0, R_0)}^{\text{Adjustment}} + \underbrace{\Delta_R F(S_1)}_{\text{Instantaneous}} \quad (7)$$

We compute total radiative forcing from this equation. The adjustment to the forcing (the change in flux

due to changes in the stratospheric temperature and the change in height of the tropopause) was computed using the first three terms. The first term was diagnosed in the main simulation, the second term diagnosed by calling the radiation code twice in the same simulation and the third term from a reference simulation. Note that the tropopause height, which has adjusted to the forcing factors, will be different from that in the reference simulation. We computed the instantaneous forcing as outlined earlier.

Note that Eqn. 7 could be rewritten as:

$$\Delta F = F^\downarrow(S_1, R_1) - F^\downarrow(S_0, R_0) + \Delta_R F^\uparrow(S_1) \quad (8)$$

i.e. the difference in downward flux between the forced and control simulations *plus* the instantaneous change in upward flux.

Variations in tropopause height are not normally considered in radiative forcing calculations. We believe that this effect should be included to the extent that the height of the tropopause changes due to changes in the stratospheric climate. Tropopause height can also vary systematically due to changes in the troposphere and is thus part of the climate system's response. Most of our computations of radiative forcing use experiments with fixed SSTs so, to first order, any changes in the tropopause are due to changes in stratospheric climate (or noise).

Forcing were diagnosed as follows:

Greenhouse gases A 15 month simulation of HadAM3 using climatological SSTs was carried out with twice pre-industrial values of CO_2 and the total forcing diagnosed from the last 12 months of that simulation. The reference state used current concentrations of CO_2 . The forcing was then scaled by $\log[\text{CO}_2]$ to obtain the time-dependent forcing. For N_2O and CH_4 single timestep simulations with each individually and with both were carried out. The forcing for each independently was scaled by the square-root of the concentration and the overlap factor computed as *Shine et al.* [1990], scaled to match the simulation in which both gases were included. The forcing from (H)(C)FCs is calculated from the *Schimmel et al.* [1995] values rescaled to give agreement with instantaneous forcing diagnosed from the full model and then to allow for a small stratospheric adjustment.

Sulphates Single-year re-runs of sections of the first HadCM3 ANTHRO simulation were used to diagnose forcing due to both the direct and indirect effects. These re-runs were carried out for the years 1860, 1900, 1950, 1975 and 2000. Three calls were made to the radiation code: the first call had the direct effect of sulphates removed, and in the second the cloud albedo perturbation was not applied. The third call was used to evolve the model simulation as in the standard HadCM3 run, and so had both effects included. Forcings were then computed from the differences between the first and third calls (direct forcing) and the second and third calls (indirect forcing), and linearly interpolated in time. No account was taken of stratospheric adjustment in these calculations.

Ozone Seasonally varying ozone for the years 1860, 1900, 1950, 1975, 1990 and 2000 used in ANTHRO simulations were used to force several simulations of HadAM3. Each simulation used seasonally varying climatological SSTs and the ozone values (both tropospheric and stratospheric) for one of the years and was integrated for three years. All other climate forcings were set to the CONTROL values. Data were discarded from the first year of each integration to allow the stratosphere to adjust and forcings computed as earlier. The stratospheric adjustment was computed by differencing the average downward tropopause fluxes from a 10-year control simulation using the same SSTs but “pre-industrial” ozone values.

Similar computations were done for tropospheric and stratospheric only ozone changes for 1975, 1990 and 1998 conditions. Forcings were then linearly interpolated in time. In 1998 we found global averages of the instantaneous forcing to be 0.04 W/m^2 , the adjustment forcing to be -0.57 W/m^2 and the total forcing to be -0.53 W/m^2 . If the calculations are done with a fixed tropopause then the instantaneous forcing is 0.10 W/m^2 and the adjustment is -0.41 W/m^2 giving a total forcing of -0.31 W/m^2 .

Natural Forcing was computed by setting the reference values of volcanic aerosol, solar irradiance and its distribution across the solar spectrum to their control values and calling the radiation code once every 15 hours throughout the coupled simulations. Sampling the forcing every 15 hours gives

good coverage of the diurnal cycle over a month. In these simulations there may be some feedbacks on the stratosphere, and thus on the adjusted fluxes, from changes in tropospheric temperatures but, as the near-surface temperature changes are generally small (Fig. 3(d)) we neglect them.

Appendix C Transformations

We use the linear transformation, A , to transform X to X' .

Given

$$X' = XA \text{ and } X'\tilde{\beta}' = X\tilde{\beta} = y$$

then

$$X(A\tilde{\beta}') = X\tilde{\beta}$$

thus

$$\tilde{\beta}' = A^{-1}\tilde{\beta}. \quad (9)$$

For example,

$$(G, SO, \text{NATURAL}) = (GHG, \text{ANTHRO}, \text{NATURAL}) \begin{pmatrix} 1 & -1 & 0 \\ 0 & 1 & 0 \\ 0 & 0 & 1 \end{pmatrix}$$

then

$$\begin{pmatrix} \tilde{\beta}_G \\ \tilde{\beta}_{SO} \\ \tilde{\beta}_{\text{NATURAL}} \end{pmatrix} = \begin{pmatrix} 1 & 1 & 0 \\ 0 & 1 & 0 \\ 0 & 0 & 1 \end{pmatrix} \begin{pmatrix} \tilde{\beta}_{\text{GHG}} \\ \tilde{\beta}_{\text{ANTHRO}} \\ \tilde{\beta}_{\text{NATURAL}} \end{pmatrix}$$

and similarly for the other transformations we use.

To obtain the transformation for $\tilde{V}(\tilde{\beta})$ pre-multiply Eqn. (2) by A^{-1} giving:

$$\begin{aligned} A^{-1}\tilde{\beta} &= A^{-1}F^T y \\ \tilde{\beta}' &= A^{-1}F^T y \\ \text{thus} \\ F'^T &= A^{-1}F^T \end{aligned}$$

$$\begin{aligned} \tilde{V}(\tilde{\beta}') &= F'^T C_{N_2} F' \\ &= A^{-1}F^T C_{N_2} F A^{-1T} \\ &= A^{-1}\tilde{V}(\tilde{\beta})A^{-1T} \end{aligned} \quad (10)$$

References

- Albrecht, B. A., Aerosols, cloud microphysics and fractional cloudiness, *Science*, 245, 1227–1230, 1989.
- Allen, M. R. and L. A. Smith, Monte Carlo SSA; detecting irregular oscillations in the presence of coloured noise, *J. Climate*, 9, 3373–3404, 1996.
- Allen, M. R. and P. A. Stott, Estimating signal amplitudes in optimal fingerprinting. part I: theory, *Cli. Dyn.*, In preparation, 2000.
- Allen, M. R. and S. F. B. Tett, Checking for model consistency in optimal fingerprinting, *Cli. Dyn.*, 15, 419–434, 1999.
- Barnett, T. P., K. Hasselmann, M. Chelliah, T. Delworth, G. Hegerl, P. Jones, E. Rasmusson, E. Roeckner, C. Ropelewski, B. Santer, and S. Tett, Detection and attribution of recent climate change: A status report, *BAMS*, pp. 2631–2659, 1999.
- Collins, M., T. J. Osborn, S. F. B. Tett, K. R. Briffa, and F. H. Schweingruber, A comparison of the variability of a climate model with a network of tree-ring densities, *J. Clim.*, (Submitted), 2000a.
- Collins, M., S. F. B. Tett, and C. Cooper, The internal climate variability of HadCM3, a version of the Hadley Centre coupled model without flux adjustments, *Clim. Dyn.*, (In press), 2000b.
- Collins, W., D. Stevenson, C. Johnson, and R. Derwent, Tropospheric ozone in a global-scale three-dimensional lagrangian model and its response to NOx emission controls, *J. Atmos. Chem.*, 26, 223–274, 1997.
- Crowley, T., Causes of climate change over the past 1000 years., *Science*, 289, 270–277, 2000.
- Dignon, J. and S. Hameed, Global emissions of nitrogen and sulfur oxides from 1860 to 1980, *J. Air Pollut. Control Assoc.*, 39, 180–186, 1990.
- Edwards, J. M. and A. Slingo, Studies with a flexible new radiation code. I: Choosing a configuration for a large-scale model, *Q. J. Roy. Meteorol. Soc.*, 122, 689–719, 1996.
- Gaffen, D., M. Sargent, R. Habermann., and J. Lanzante, Sensitivity of tropospheric and stratospheric temperature trends to radiosonde data quality, *J. Clim.*, 13, 1776–1796, 2000.
- Gordon, C., C. Cooper, C. A. Senior, H. Banks, J. M. Gregory, T. C. Johns, J. F. B. Mitchell, and R. A. Wood, The simulation of SST, sea ice extents and ocean heat transports in a version of the Hadley Centre coupled model without flux adjustments, *Climate Dyn.*, 16, 147–168, 2000.
- Haigh, J. D., The role of stratospheric ozone in modulating the solar radiative forcing of climate, *Nature*, 370, 544–546, 1994.
- Haigh, J. D., Impact of solar variability on climate, *Science*, 272, 981–984, 1996.
- Hansen, J., M. Sato, and R. Reudy, Radiative forcing and climate response, *J. Geophys. Res.*, 102, 6831–6864, 1997.
- Hasselmann, K., On the signal-to-noise problem in atmospheric response studies., in *Meteorology over the tropical oceans*, edited by D. B. Shaw, pp. 251–259, Royal Meteorological Society, 1979.
- Hasselmann, K., Optimal fingerprints for the detection of time-dependent climate change, *J. Clim.*, 6, 1957–1971, 1993.
- Hasselmann, K., Multi-pattern fingerprint method for detection and attribution of climate change, *Cli. Dyn.*, 13, 601–611, 1997.
- Hegerl, G. C., K. Hasselmann, U. Cubasch, J. F. B. Mitchell, E. Roeckner, R. Voss, and J. Wizejwitz, Multi-fingerprint detection and attribution analysis of greenhouse gas, greenhouse gas-plus-aerosol and solar forced climate change., *Cli. Dyn.*, 13, 613–634, 1997.
- Hegerl, G. C., P. D. Jones, and T. P. Barnett, Effect of observational sampling error on the detection of anthropogenic climate change, *J. Clim.*, (in press), 2000a.
- Hegerl, G. C. and G. R. North, Comparison of statistically optimal approaches to detecting anthropogenic climate change, *J. Clim.*, 10, 1125–1133, 1997.
- Hegerl, G. C., P. A. Stott, M. R. Allen, J. F. B. Mitchell, S. F. Tett, and U. Cubasch, Optimal detection and attribution of climate change: Sensitivity of results to climate model differences, *Cli. Dyn.*, (in press), 2000b.
- Hill, D., N. Gillett, M. Allen, P. Stott, and S. Tett, Detection of a solar signal in recent atmospheric vertical temperature structure, *J. Geophys. Res.*, (In Prep.), 2000.
- Hoyt, D. V. and K. H. Schatten, A discussion of plausible solar irradiance variations, 1700–1992., *J. Geophys. Res.*, 98, 18895–18906, 1993.
- Johns, T. C., R. E. Carnell, J. F. Crossley, J. M. Gregory, J. F. B. Mitchell, C. A. Senior, S. F. B. Tett, and R. A. Wood, The second Hadley Centre coupled ocean-atmosphere GCM: Model description, spinup and validation, *Cli. Dyn.*, 13, 103–134, 1997.
- Johns, T. C., W. J. Ingram, C. E. Johnson, A. Jones, J. F. B. Mitchell, D. L. Roberts, D. M. H. Sexton, D. S. Stevenson, S. F. B. Tett, and M. J. Woodage, Anthropogenic climate

- change for 1860 to 2100 simulated with the HadCM3 model under updated emissions scenarios, In preparation, 2000.
- Jones, A., D. L. Roberts, and M. J. Woodage., The indirect effects of anthropogenic sulphate aerosol simulated using a climate model with an interactive sulphur cycle., HCTN-14, Hadley Centre, The Met. Office, London Rd, Bracknell, Berks, RG12 2SY, 1999.
- Kattenberg, A., F. Giorgi, H. Grassl, G. A. Meehl, J. F. B. Mitchell, R. J. Stouffer, T. Tokioka, A. J. Weaver, and T. M. L. Wigley, Climate models—projections of future climate, in *Climate Change 1995. The Science of Climate Change*, edited by J. T. Houghton, L. G. Meira Filho, B. A. Callander, N. Harris, A. Kattenberg, and K. Maskell, chapter 6, pp. 285–358, Cambridge University Press, Cambridge, 1996.
- Lacis, A., J. Hansen, and M. Sato, Climate forcing by stratospheric aerosols, *GRL*, 19, 1607–1610, 1992.
- Lean, J., J. Beer, and R. Bradley, Reconstruction of solar irradiance since 1610: implications for climate change, *Geophys Res Lett*, 22, 3195–3198, 1995a.
- Lean, J. L., O. R. White, and A. Skumanich, On the solar ultraviolet spectral irradiance during the Maunder Minimum, *Global Biogeochemical Cycles*, 9, 171–182, 1995b.
- Mann, M. E., R. S. Bradley, and M. K. Hughes, Global-scale temperature patterns and climate forcing over the past six centuries, *Nature*, 392, 779–787, 1998.
- Mardia, K. V., J. T. Kent, and J. M. Bibby, *Multivariate Analysis*, Academic Press, 1979.
- Nakićenović, N., J. Alcamo, G. Davis, B. de Vries, J. Fenhann, S. Gaffin, K. Gregory, A. Grübler, T. Y. Jung, T. Kram, E. L. La Rovere, L. Michaelis, S. Mori, T. Morita, W. Pepper, H. Pitcher, L. Price, K. Riahi, A. Roehrl, H.-H. Rogner, A. Sankovski, M. Schlesinger, P. Shukla, S. Smith, R. Swart, S. van Rooijen, V. Nadejda, and Z. Dadi, *Special report on emissions scenarios*, Cambridge, 599pp, 2000.
- North, G. R. and K.-K. Kim, Detection of forced climate signals. Part II: simulation results, *J. Clim.*, 8, 409–417, 1995.
- North, G. R., K.-K. Kim, S. S. P. Shen, and J. W. Hardin, Detection of forced climate signals. Part I: filter theory, *J. Clim.*, 8, 401–408, 1995.
- North, G. R. and M. J. Stevens, Detecting climate signals in the surface temperature record., *J. Clim.*, 11, 563–577, 1998.
- Orn, G., U. Hansson, and H. Rodhe, Historical worldwide emissions of anthropogenic sulfur: 1860–1985, Technical Report CM-91, Stockholm University, 1996.
- Parker, D., M. Gordon, D. Cullum, D. Sexton, C. Folland, and N. Rayner, A new global gridded radiosonde temperature data base and recent temperature trends, *Geo. Res. Lett.*, 24, 1499–1502, 1997.
- Parker, D. E., P. D. Jones, C. K. Folland, and A. Bevan, Interdecadal changes of surface temperature since the late nineteenth century, *J. Geophys. Res.*, 99, 14373–14399, 1994.
- Pope, V. D., M. L. Gallani, P. R. Rowntree, and R. A. Stratton, The impact of new physical parametrizations in the Hadley Centre climate model – HadAM3, *Climate Dyn.*, 16, 123–146, 2000.
- Randel, W. J. and F. Wu, A stratospheric ozone trends data set for global modelling studies, *GRL*, 26, 3089–3092, 1999.
- Rowell, D. P., Assessing potential seasonal predictability with an ensemble of multidecadal GCM simulations, *J. Clim.*, 11, 109–120, 1998.
- Salby, M. and P. Callaghan, Connection between the solar cycle and the QBO: the missing link, *J. Geophys. Res.*, 105, 2652–2662, 2000.
- Santer, B. D., K. E. Taylor, T. M. Wigley, T. C. Johns, P. D. Jones, D. J. Karoly, J. F. B. Mitchell, A. H. Oort, J. E. Penner, V. Ramaswamy, M. D. Schwarzkopf, R. J. Stouffer, and S. Tett, A search for human influences on the thermal structure of the atmosphere, *Nature*, 382, 39–45, 1996.
- Sato, M., J. E. Hansen, M. P. McCormick, and J. B. Pollack, Stratospheric aerosol optical depths (1850–1990), *J. Geophys. Res.*, 98, 22987–22994, 1993.
- Schimel, D., D. Alves, I. Enting, M. Heimann, F. Joos, D. Raynaud, T. Wigley, M. Prather, R. Derwent, D. Enhalt, P. Fraser, E. Sanhueza, X. Zhou, P. Jonas, R. Charlson, H. Rodhe, S. Sadasivan, K. P. Shine, Y. Fouquart, V. Ramaswamy, S. Solomon, J. Srinivasan, D. Albritton, R. Derwent, I. Isaksen, M. Lal, and D. Wuebbles, Radiative forcing of climate change, in *Climate Change 1995. The Science of Climate Change*, edited by J. T. Houghton, L. G. M. Filho, B. A. Callander, N. Harris, A. Kattenberg, and K. Maskell, chapter 2, pp. 65–131, Cambridge University Press, Cambridge, 1995.
- Shine, K., R. Derwent, D. Wuebbles, and J.-J. Morcrette, Radiative forcing of climate, in *Climate Change. The IPCC scientific assessment*, edited by J. Houghton, G. Jenkins, and J. Ephraums, chapter 5, pp. 45–68, Cambridge University Press, Cambridge, 1990.
- Shine, K. P., Y. Fouquart, V. Ramaswamy, S. Solomon, and J. Srinivasan, *Climate Change 1994*, chapter 4 Radiative Forcing, pp. 168–203, CUP, 1995.
- Stott, P. A. and S. F. B. Tett, Scale-dependent detection of climate change, *J. Clim.*, 11, 3282–3294, 1998.

Stott, P. A., S. F. B. Tett, G. S. Jones, M. R. Allen, W. J. Ingram, and J. F. B. Mitchell, Attribution of twentieth century temperature change to natural and anthropogenic causes, *Cli. Dyn.*, (to appear), 2000.

Tett, S. F. B., J. F. B. Mitchell, D. E. Parker, and M. R. Allen, Human influence on the atmospheric vertical temperature structure: Detection and observations, *Science*, 247, 1170–1173, 1996.

Tett, S. F. B., P. A. Stott, M. R. Allen, W. J. Ingram, and J. F. B. Mitchell, Causes of twentieth century temperature change near the earth's surface, *Nature*, 399, 569–572, 1999.

Twomey, S. A., Pollution and the planetary albedo, *Atmos. Environ.*, 8, 1251–1256, 1974.

Williams, K. D., C. A. Senior, and J. F. B. Mitchell, Transient climate change in the Hadley Centre models: The role of physical processes, *J. Climate*, Submitted, 2000.

Wilson, D. and S. Ballard, A microphysically based precipitation scheme for the UK Meteorological Office Unified Model, *Quart. J. Royal Meteor. Soc.*, 125, 1607–1636, 1999.

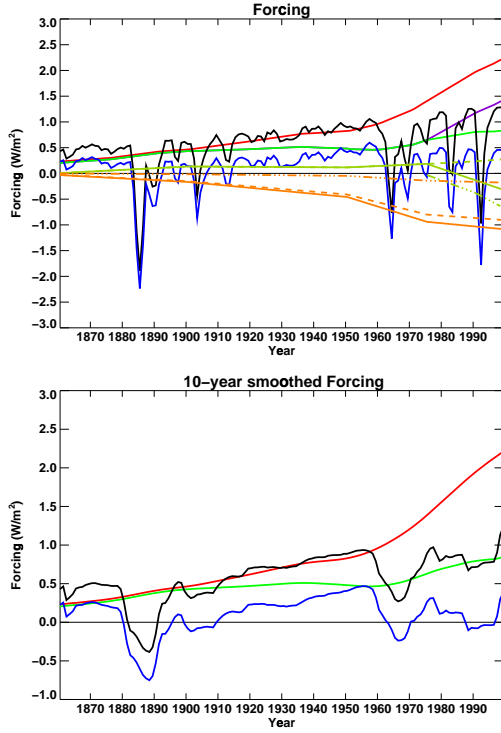


Figure 1: Global-mean forcing

a) Annual mean radiative forcings for GHG (red), TROP-ANTHRO (purple), ANTHRO (green) and the NATURAL (blue). Anthropogenic forcings are shown relative to pre-industrial times, natural forcing relative to its time mean.

The total forcing computed by summing the NATURAL and ANTHRO forcings is shown in black. Also shown is the total forcing due to sulphates (solid orange), and the direct (dot-dashed orange line) and indirect (dashed orange) effects; total ozone changes (pale green line), tropospheric ozone changes (dashed pale green line) and stratospheric ozone changes (dot-dashed green line) with the latter two only being shown for the period 1975–1998.

b) 10-year smoothed forcings for GHG, ANTHRO, NATURAL and the total forcing (colours as above).

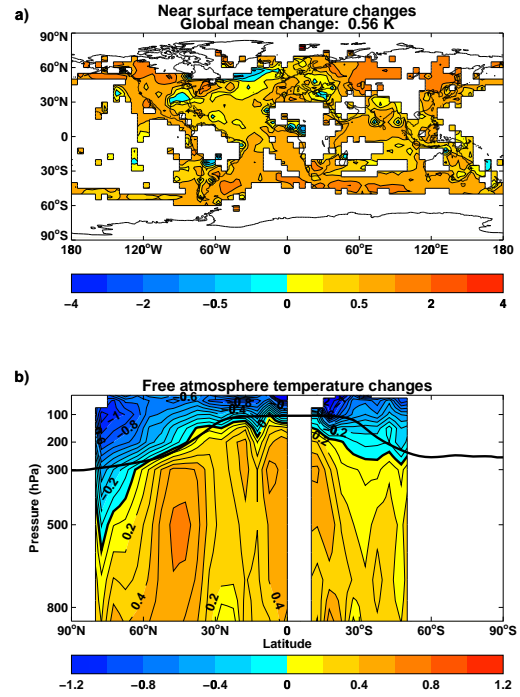


Figure 2: Observed temperature changes

a): Observed changes in near-surface temperature (1977–97 minus 1881–1920). A contour interval of 1K is used from -4K to 4K with additional contours at $\pm 0.5K$ and $\pm 0.25K$.

b): Observed changes in zonal-mean temperature (1985–95 minus 1961–80). A contour interval of 0.1K is used with every second contour labelled from -1.2K to 1.2K. The black line denotes the zonal-mean position of the tropopause from the NCEP/NCAR reanalysis for the period 1985–95 using data provided by the NOAA-CIRES Climate Diagnostics Center, Boulder, Colorado, from <http://www.cdc.noaa.gov/>.

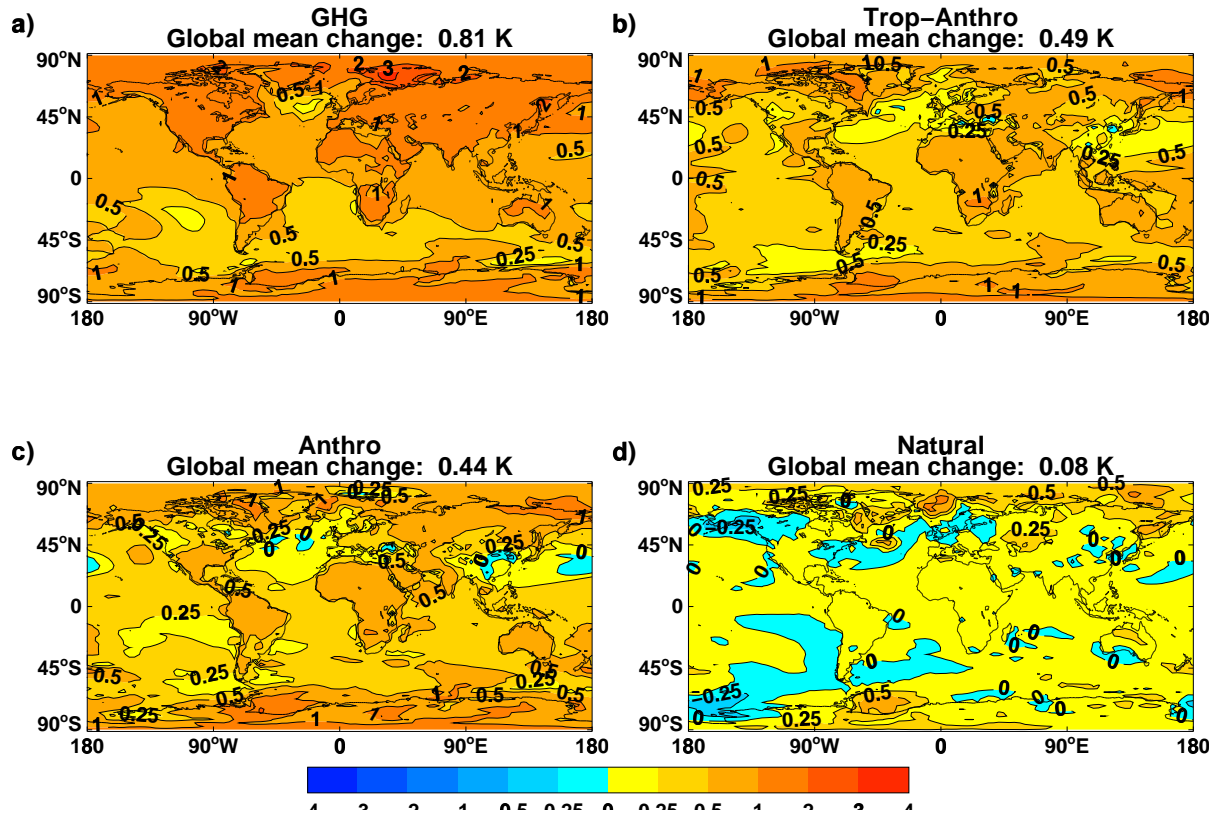


Figure 4: Simulated 20th century temperature changes.

Temperature difference (K) between the 20-year average 1977–1997 and the 40-year average 1881–1920 for the four ensembles, GHG (a), TROP-ANTHRO (b), ANTHRO (c), and NATURAL (d). Note these plots show the *raw* model data (i.e. without the observed mask). All other details are as Fig.2(a).

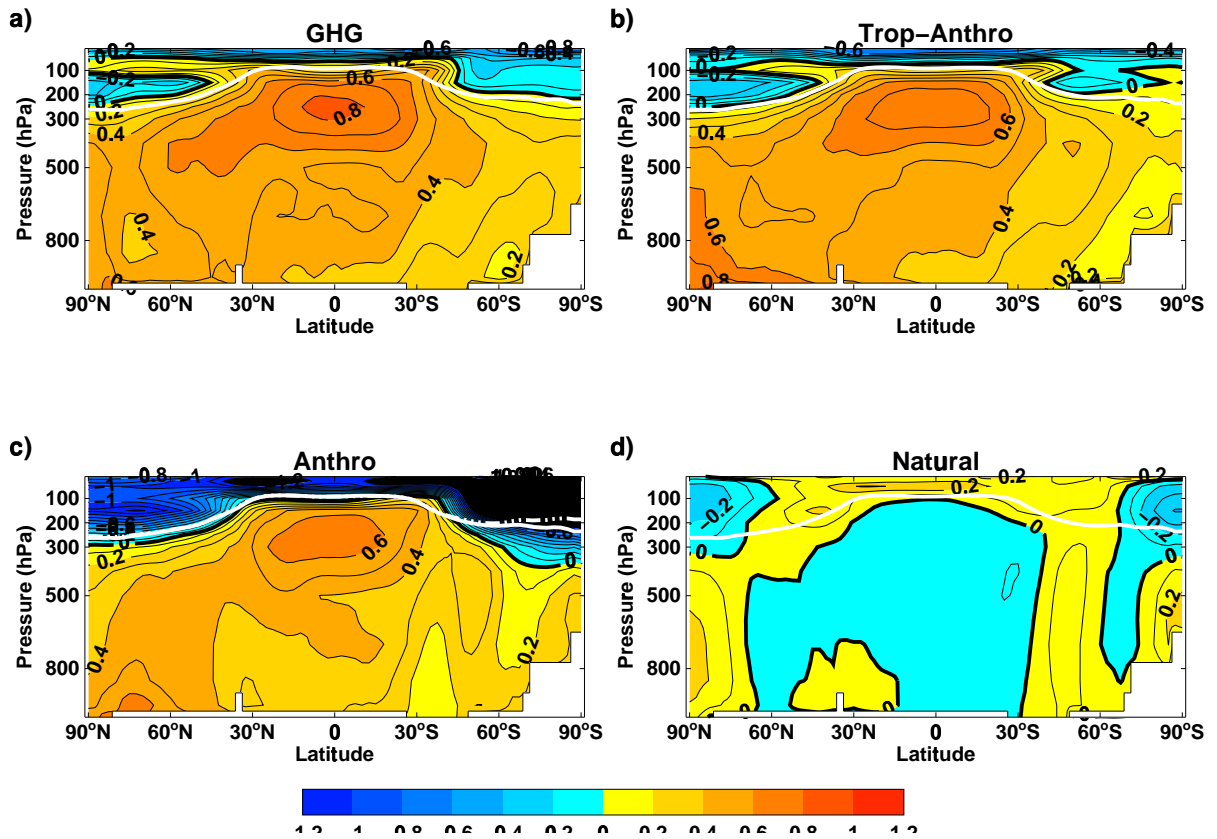


Figure 5: Simulated zonal-mean temperature differences
Differences (K) between 1985–1995 and 1961–1980 for the four ensembles: GHG (a), TROP-ANTHRO (b) ANTHRO (c) and NATURAL (d). White lines show the position of the mean tropopause in CONTROL while the dashed white line in (c) shows the mean position of the tropopause in a atmosphere only simulation with 1990 stratospheric ozone. The maximum difference between the two lines is approximately 50 hPa. All other details are as Fig. 2 (b).

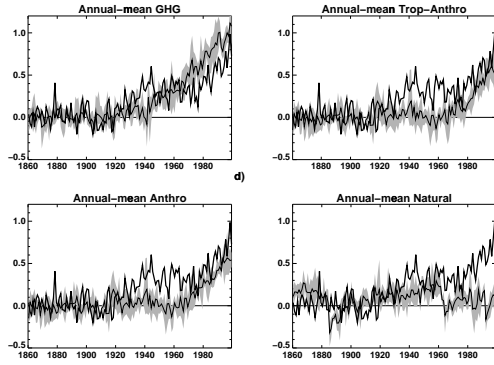


Figure 3: Global-mean near-surface temperature changes

Near-surface changes in global-mean temperature, relative to the 1881–1920 mean for the observations (thick black line) and the ensemble-mean of the GHG(a), TROP-ANTHRO(b), ANTHRO(c) and NATURAL(d) simulations (thin black line). The maximum and minimum range from the individual simulations is shown in gray.

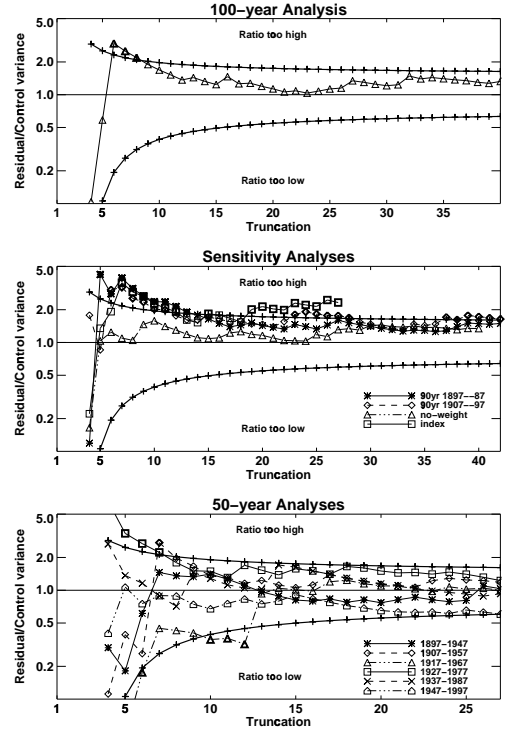


Figure 6: Residual variances for surface analyses
Ratio of the residual to control variance using a logarithmic scale (solid line with triangles) for the century analysis (a), four sensitivity studies (b) and all six 50-year analyses of surface temperature (c). Also shown in is the 10–90% values of the ratio under the null hypothesis that CONTROL and residual variances are the same (solid lines with + symbols). Note that CONTROL variance has been inflated (see Section 4.1 for details). Bold symbols show values outside these limits.

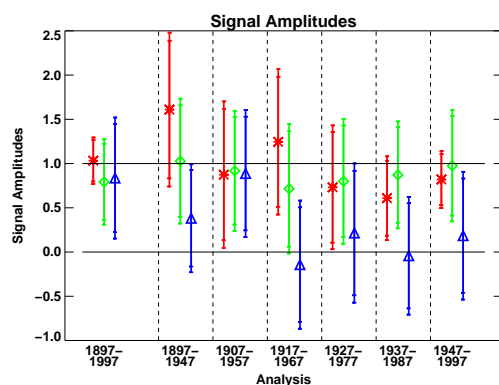


Figure 7: Signal amplitudes and uncertainties

Amplitudes and uncertainty ranges for 100-year analysis and all 50-year analyses for *G* (left red error bar with asterisk), *SO* (centre green error bar with diamond), *NATURAL* (right blue error bar with triangle). The error bars show the 5–95% uncertainty ranges for “detection” (inner) and “amplitude-consistency” (outer). The best-estimate signal amplitude is shown as a symbol at the centre of the bar.

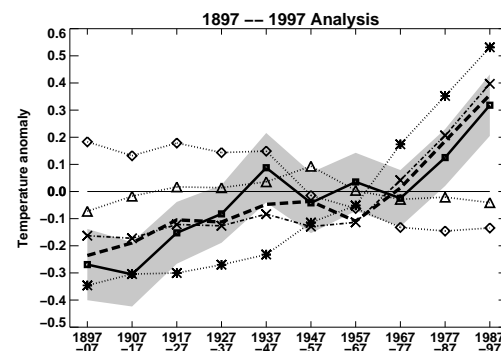


Figure 8: 100-year best-estimate reconstruction of near-surface temperature changes

Reconstruction of temperature variations for 1897–1997. Observed (solid line with squares), best-estimate (heavy dashed line) changes and best-estimate contributions from *G* (dotted line with asterisks), *SO* (dotted line with diamonds), *NATURAL* (dotted line with triangles). Also shown is the best-estimate total anthropogenic contribution (dot-dashed line with crosses). All timeseries were reconstructed from data in which the 100-year mean had first been removed. The grey region centred on the observations shows the uncertainty range due to internal variability (two sigma decadal variability computed from C_{N_2}).

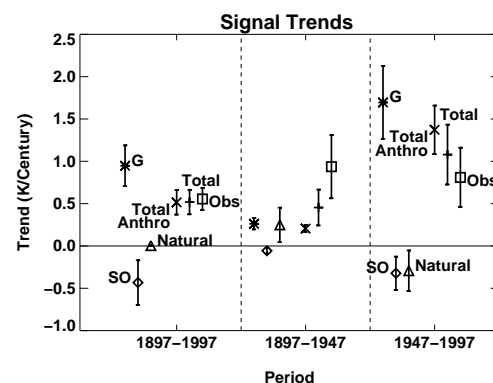


Figure 9: Linear trends from century analysis

Best-estimate linear trend and uncertainty ranges (K/century). Symbols as Fig. 7 with the addition of total anthropogenic trend (x), total trend (+) and observed trends (square). Symbols show best-estimate trend whilst error bars show the 5–95% uncertainty range inflated to allow for four member ensembles.

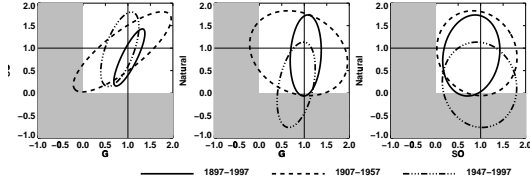


Figure 10: Joint confidence regions

90% joint confidence regions for the 1897–1997 (solid), 1907–1957 (dashed) and 1947–1997 (dot-dashed) from G SO NATURAL analysis. Shown are the two-dimensional confidence regions for G SO (a), G NATURAL (b) and SO NATURAL (c). Points inside the ellipse are consistent with (1, 1).

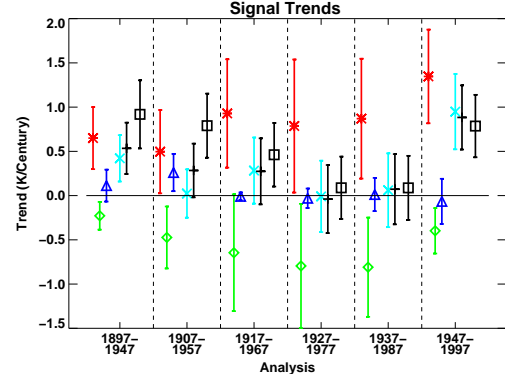


Figure 12: 50-year linear trends and uncertainties

Best-estimate linear-trend and uncertainty ranges (K/century) for 50-year timescale analysis. Colours and symbols as Fig. 7 with the addition of total anthropogenic trend (pale blue x), total trend (black +) and observed trends (black square).

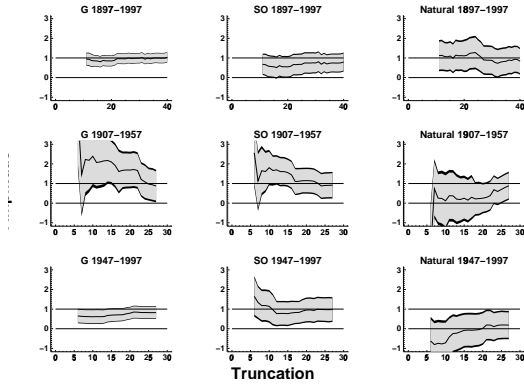


Figure 11: Signal amplitudes and uncertainties, as a function of truncation, for near-surface analyses.

The best-estimate amplitudes (solid line), 5–95% “detection” uncertainties (light-grey shading) and 5–95% “amplitude-consistency” uncertainties (thin band of black) are shown for the 1897–1997 analysis (top row) and two 50-year analyses (1907–1957 and 1947–1997) (bottom two rows) for G (left column), SO (centre column) and NATURAL (right column) as a function of truncation.

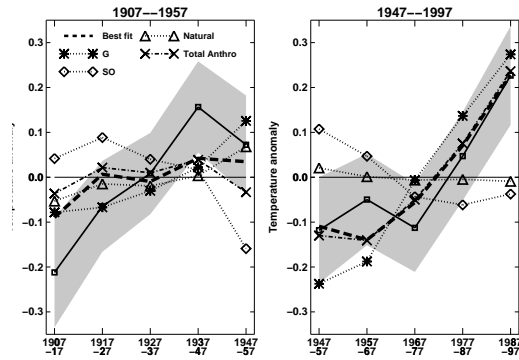


Figure 13: 50-year best-estimate reconstruction of near-surface temperature changes

Best-estimate reconstruction of temperature variations for 1907–1957 (a) and 1947–97 (b). As Fig. 8 but reconstructed from data from which the 50-year mean had first been removed.

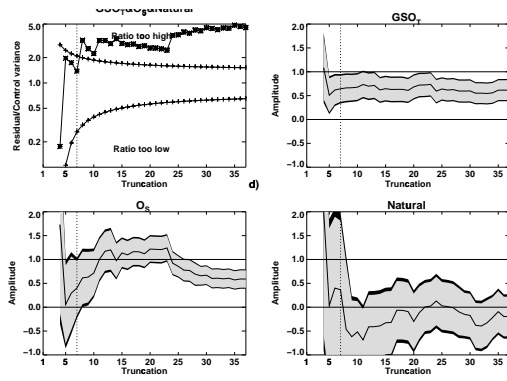


Figure 14: Sensitivity to truncation for free atmosphere analysis.

The ratio of the residual to the CONTROL variance (solid line with asterisks), using a logarithmic scale, is plotted in (a). Other details of plot are as Fig. 6. Note that CONTROL variance has been inflated (see Section 4 for details). The vertical dotted line shows truncation seven – the largest truncation for which the residual and CONTROL variance are consistent.

Shown as a function of truncation are the best-estimate amplitudes (solid line), 5–95% “detection” uncertainties (light-gray shading), 5–95% “amplitude-consistency” uncertainties (thin black shading) for GSO_T (b) and O_S (c).

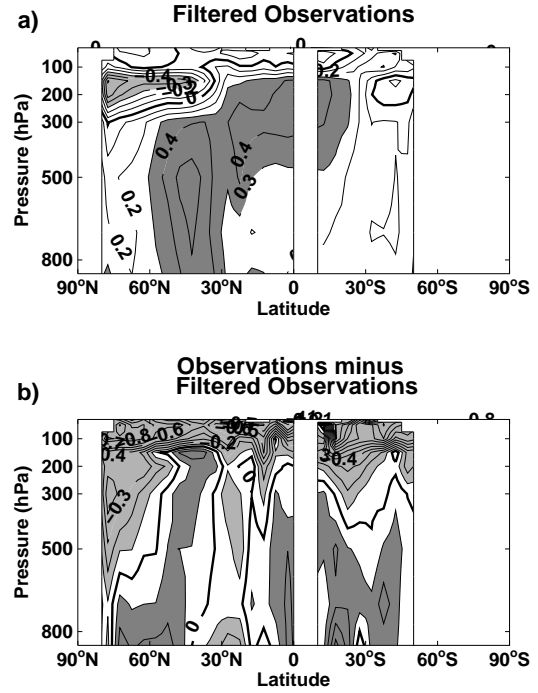


Figure 15: Filtered observations

a: Observed changes in zonal mean temperature filtered by projection onto the leading seven eigenvectors of C_N . A contour interval of 0.1 is used with dark (light) shading for values above (below) 0.3K (-0.3K) and the zero contour drawn bold.

b: Raw observations minus (a) (i.e. what the filtering removes). A contour interval of 0.1K is used with dark (light) shading for values above (below) 0.1K (-0.1K). The zero contour is drawn bold.

Case	Period	Trunc.	% Var.	GHG	T-A	ANTHRO	NATURAL	ν_1	ν_2
Surface (century)	1897–97	40	96.4	5.85	3.77	3.35	1.17*	40	27
	1897–97	20	91.3	7.45	4.50	3.93	1.43	40	27
No-weight	1897–97	40	83.2	5.06	–	2.72	1.16*	40	27
	1897–97	20	65.9	6.17	–	3.01	1.36	40	27
Index	1897–97	18 [†]	98.0	6.42	–	3.75	1.39	40	27
	1897–97	9	67.0	7.82	–	3.78	1.43	40	27
90-year	1897–87	36 [†]	94.9	4.47	–	2.33	1.14*	42	27
	1897–87	19	91.7	5.72	–	2.77	1.35	42	27
	1907–97	36 [†]	96.0	5.60	–	3.32	1.01*	42	27
	1907–97	19	91.7	6.93	–	3.86	1.17*	42	27
Surface (50-year)	1897–47	27	95.6	1.54	–	1.35	1.37	27	33
	1907–57	27	95.1	1.92	–	1.29	1.44	27	33
	1917–67	27	94.1	2.21	–	1.23*	1.39	27	33
	1927–77	27	91.8	3.01	–	1.70	1.59	27	33
	1937–87	27	86.3	3.97	2.76	2.34	1.57	27	33
	1947–97	27	92.9	4.79	4.37	3.66	1.60	27	33
Free Atmos.	1961–95	7 [†]	48.0	–	6.11	5.90	0.97*	36	42

Table 1: Signal properties

Shown for each analysis are the truncation used (third column), and the fraction of the observed variance (after processing) after filtering in the truncated eigenvector space (fourth column). By processing we mean, for example, projection onto spherical harmonics and weighting by $\sqrt{(1/2l+1)}$ for the surface analyses and, zonal-meaning and mass weighting for the free atmosphere analysis. [†] denotes cases in which the truncation used is less than the largest possible. Cases in *italic* are when tests for signal degeneracy suggest that the three-signal combination is degenerate.

The centre columns show the signal-to-noise ratio (SNR—see Section 4.6 for details) of the simulated signals. T-A (TROP-ANTHRO) is identical to ANTHRO before 1975. Therefore results from TROP-ANTHRO are not shown for those 50-years analyses before 1937–77 and for the sensitivity analyses. SNR values shown with a * are where the value is not significantly different, at the 90% level, from unity (that expected by chance) suggesting significant noise contamination of that simulated signal.

Shown in the right-hand columns are the estimated dof of C_N (ν_1) and C_{N_2} (ν_2).

Case	Truncation	Signal Amplitude		
		G	SO	NATURAL
Century	40	1.03✓	0.79✓	0.84✓
Century	20	0.85✓	0.55✓	1.11✓
No-weight	40	0.96✓	0.67✓	0.87✓
No-weight	20	0.79✓	0.49	1.03✓
Index	18	0.96✓	0.83✓	0.60
<i>Index</i>	9	0.77✓	0.58✓	0.70
90-year 1897–1987	36	0.95✓	0.71✓	1.05✓
90-year 1897–1987	19	0.79✓	0.50	1.07✓
<i>90-year 1907–1997</i>	36	1.03✓	0.89✓	0.70✓
<i>90-year 1907–1997</i>	19	0.86✓	0.63✓	0.97✓

Table 2: Sensitivity studies

The best-estimate signal amplitudes for the base analysis (century) and sensitivity studies are shown. Detectable signals are denoted by a ✓ and when the signal amplitude is inconsistent with unity a * is shown. Cases in *italic* are when tests for signal degeneracy suggest that the three-signal combination is degenerate. The dof used in the tests are given in Table 1.

Case	Truncation	Amplitude/Uncertainty		
		G	SO	NATURAL
Century	40	4.40	1.84	1.37
Century	20	3.40	1.11	1.49
No-weight	40	3.61	1.44	1.52
No-weight	20	2.73	0.98	1.45
Index	18	3.84	1.82	0.95
<i>Index</i>	9	2.26	1.19	0.78
90-year 1897–1987	36	3.07	1.54	1.93
90-year 1897–1987	19	2.47	0.91	1.51
<i>90-year 1907–1997</i>	36	4.22	1.93	1.04
<i>90-year 1907–1997</i>	19	3.28	1.21	1.05

Table 3: Ratio of signal amplitudes to uncertainty range

Shown, for the sensitivity studies and base century analysis, are the ratio of the best-estimate signal amplitudes to half the uncertainty range. Inflating the simulated variability by this factor (scaling C_{N_2} by it squared) makes the signal amplitude consistent with zero at the 5% level. Where the factor is greater than unity then it is the minimum amount needed to inflate the simulated variability so that the signal is no longer detected.